

June 1996

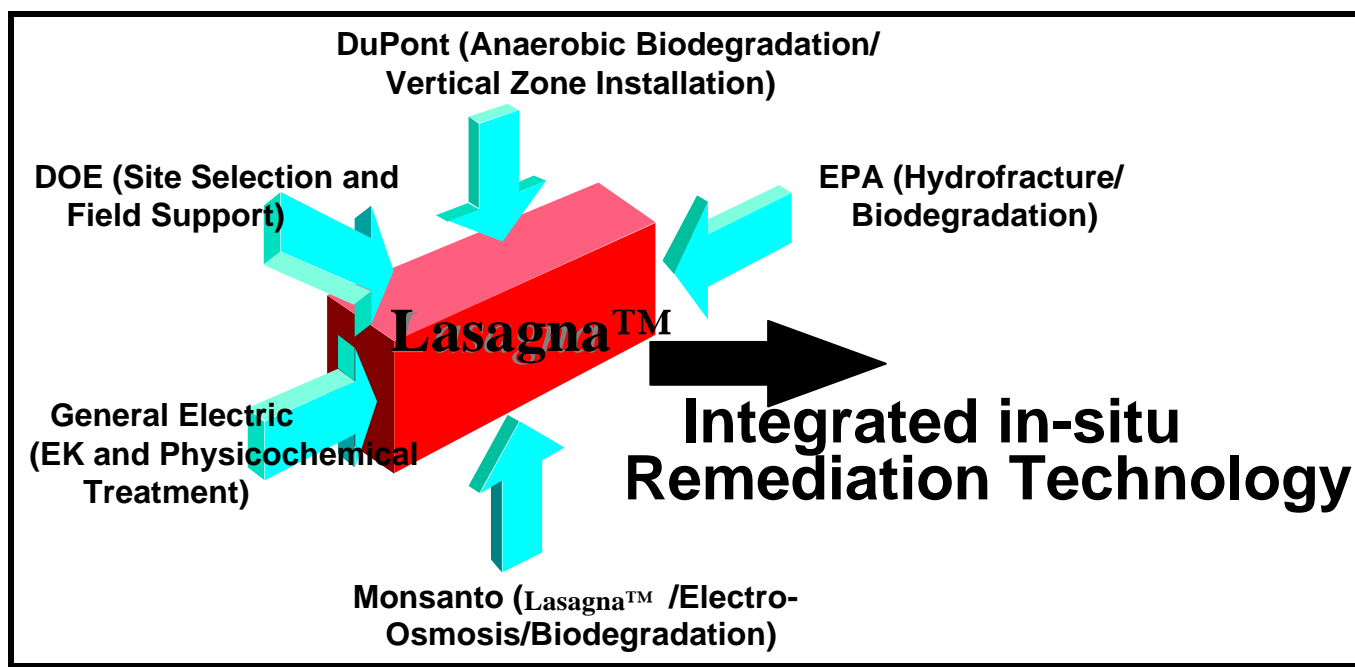


Development of an Integrated in-situ Remediation Technology

Topical Report for *Tasks No. 2-4* entitled “*Electrokinetic Modeling*” (September 26, 1994 -May 25, 1996)

Andrew P. Shapiro (General Electric Research and Development)

DOE Contract Number: DE-AR21-94MC31185



Submitted to:

U. S. Department of Energy
Morgantown Energy Technology Center
Morgantown, West Virginia

Submitted by:

General Electric Company
Schenectady, New York

and

Monsanto Company
800 N. Lindbergh Boulevard
St. Louis, Missouri 63167

Monsanto



"The Key to Environmental Safety"

Monsanto Company
800 N. Lindbergh Boulevard
St. Louis, Missouri 63167
Phone: (314) 694-1466
FAX: (314) 694-1531

20 March, 1997

Re: Ordering Information for "*Development of an Integrated in-situ Remediation Technology*"
Topical Reports generated under DOE contract number DE-AR21-94MC31185 which was
signed September 26, 1994.

Dear Sir/Ms.:

The following table summarizes ordering information for all technical reports written for the above referenced contract. Copies of these reports may be obtained from the Office of Scientific and Technical Information [(423)576-8401] if you are with DOE or a DOE contractor, or from:

National Technical Information Service (NTIS)
5285 Port Royal Road
Springfield, VA 22161
Phone: (703)487-4600 (Regular Service)
Phone: (703)487-4700 (Rush Service, \$10.00 Additional Per Item)

(continued on next page)

Title	Document Number
<ul style="list-style-type: none"> • Topical Report for Task #1 entitled "Evaluation of Treatment Zone Formation Options" (September 26, 1994 - May 25, 1996) Stephen H. Shoemaker, Richard C. Landis, Ronald J. Griffith, Dale S. Schultz, and Gary E. Quinton (DuPont Company) 	DOE/METC/31185 —5436, DE97002165
<ul style="list-style-type: none"> • Topical Report for Tasks #2-4 entitled "Electrokinetic Modeling" (September 26, 1994 - May 25, 1996) Andrew P. Shapiro (General Electric Company) 	DOE/METC/31185 —5391, DE97002135
<ul style="list-style-type: none"> • Topical Report for Task #5 entitled "Cost Analysis" (September 26, 1994 - May 25, 1996) Gary Quinton, Dale Schultz, Richard Landis, Ronald Griffith, and Stephen Shoemaker (DuPont Company) 	DOE/METC/31185 —5389, DE97002134
<ul style="list-style-type: none"> • Topical Report for Task #6 entitled "Lab-Scale Development of Microbial Degradation Process" (September 26, 1994 - May 25, 1996) J. Martin Odom (DuPont Company) 	DOE/METC/31185 —5388, DE97002130
<ul style="list-style-type: none"> • Topical Report for Task #7 entitled "Development of Degradation Processes" (September 26, 1994 - May 25, 1996) M. J. Brackin, M. H. Heitkamp and S. V. Ho (Monsanto Company) 	DOE/METC/31185 —5495, DE97002165
<ul style="list-style-type: none"> • Topical Report for Tasks #8 and 10 entitled "Laboratory and Pilot Scale Experiments of the <i>Lasagna</i>TM Process" (September 26, 1994 - May 25, 1996) Sa V. Ho, Christopher J. Athmer, and P. Wayne Sheridan (Monsanto Company) and Andrew P. Shapiro (General Electric Company) 	DOE/METC/31185 —5375, DE97002150
<ul style="list-style-type: none"> • Topical Report for Task #9-Part I entitled "TCE Degradation Using Non-Biological Methods" (September 26, 1994 - May 25, 1996) Andrew P. Shapiro, Timothy M. Sivavec, and Sunita S. Baghel (General Electric Company) 	DOE/METC/31185 —5392, DE97002133
<ul style="list-style-type: none"> • Topical Report for Task #9 - Part II entitled "TCE Degradation Using Non-Biological Methods" (September 26, 1994 - May 25, 1996) Robert G. Orth and David E. McKenzie (Monsanto Company) 	DOE/METC/31185 —5393, DE97002131

(continued on next page)

<ul style="list-style-type: none">• Topical Report for Task #11 entitled "Evaluation of TCE Contamination Before and After the Field Experiment" (September 26, 1994 - May 25, 1996) B. Mason Hughes, Sa V. Ho, Christopher J. Athmer, and P. Wayne Sheridan (Monsanto Company) Stephen H. Shoemaker and John R. Larson (DuPont) Jay L. Clausen (LMES) and John L. Zutman (ORNL-Grand Junction)	DOE/METC/31185 —5496, DE97002166
<ul style="list-style-type: none">• Topical Report for Tasks #12 and 13 entitled "Large Scale Field Test of the <i>Lasagna</i>TM Process" (September 26, 1994 - May 25, 1996) Christopher J. Athmer, Sa V. Ho, B. Mason Hughes, P. Wayne Sheridan, and P. H. Brodsky (Monsanto Company) Andrew P. Shapiro, Roy F. Thornton, and Joseph J. Salvo (General Electric Company) and Dale S. Schultz, Richard C. Landis, Ron Griffith, and Stephen H. Shoemaker (DuPont)	DOE/METC/31185 —5390, DE97002156

Development of an Integrated in situ Remediation Technology

DOE Contract Number: DE-AR21-94MC31185

Topical Report for *Tasks No. 2-4 Electrokinetic Modeling*

Andrew P. Shapiro
General Electric Research and Development
P.O. Box 8
Schenectady, NY 12309

Submitted by

Monsanto Company
St. Louis, Missouri

and

General Electric Company
Schenectady, New York

Abstract: Contamination in low-permeability soils poses a significant technical challenge for in situ remediation efforts. Poor accessibility to the contaminants and difficulty in delivery of treatment reagents have rendered existing in situ treatments such as bioremediation, vapor extraction, and pump and treat rather ineffective when applied to low-permeability soils present at many contaminated sites. The LasagnaTM technology is an integrated in situ treatment in which established geotechnical methods are used to install degradation zones directly in the contaminated soil and electro-osmosis is used to move the contaminants back and forth through those zones until the treatment is completed. The present Draft Topical Report for Tasks No. 2-4 summarizes the modeling of electrokinetic remediation conducted by General Electric Company. The report presents analyses on thermal behavior of electrokinetic remediation, chemical species transport, and electrode geometry and soil heterogeneity. The mathematical models presented in this report are validated by comparison with experimental data. These models will serve as tools for scaling up the Lasagna process.

TM Lasagna is a trademark of the Monsanto Company.

Table of Contents

Section	page
Abstract	iii
Table of Contents	v
List of Figures	vi
List of Tables	viii
A Executive Summary	1
B Background	3
Statement of Work	3
The Solution	3
Consortium Description	3
Management Plan	3
Technical Deliverables	3
C Draft Topical Report for Tasks No. 2-4	5
1. Thermal Model	5
2. Chemical Species Model	15
Transport Model	19
References	19
3. Analysis of Electrode Geometry and Heterogeneity	39
D Acronyms and Abbreviations	44
E. Units	46

List of Figures

Figure	page
1. Comparison of temperature dependence of water viscosity and electrical conductivity of soil	7
2. Geometry for computer simulations.	7
3. Maximum temperature vs time for three simulated cases.....	9
4. Power consumption vs time for three simulated cases	9
5. Pore volume moved through soil	10
6. Comparison of model predictions of temperatures	10
7. Comparison of model prediction and field test data of power consumption vs time.....	11
8. Maximum temperature rise vs time	13
9. Pore volumes removed vs time	13
10. Applied voltage vs time.	14
11. Adsorbed H ⁺ concentration vs pH determined from titration data	17
12. Application of the model to Paducah soil	18
13. Titration curve for 2% solution of agar gel	22
14a. pH distribution for agar simulation with inert anode	23
14b. Pore water ion distribution for agar simulation with inert anode	23
14b. Pore water ion distribution for agar simulation with inert anode	24
14d. Trajectory of high and low pH fronts for agar simulation with inert anode	24
15. Model prediction of electric field in agar experiments	25
16a. pH distribution for agar simulation with iron anode	28
16b. Pore water ion distribution for agar simulation with iron anode	28
16c. Voltage profile for agar simulation with iron anode	29
16d. Trajectory of high and low pH fronts for agar simulation with iron anode	29
17. Comparison of model prediction and measured total iron distribution in agar experiments with iron anode	30
18. Comparison of experimental and predicted anolyte and catholyte pH behavior in agar experiments	31
19a. pH distribution (0-3 m) for simulation of Paducah field test with inert anodes	33
19b. pH distribution (0-0.3 m) for simulation of Paducah field test with inert anodes.	33
19c. Pore water ion distribution (0-3 m) for simulation of Paducah field test with inert anodes	34
19d. Pore water ion distribution (0-0.3 m) for simulation of Paducah field test with inert anodes	34
20. System resistance predicted by model simulation and experimental data of Paducah pilot test	35

21.	Voltage distribution for simulation of Paducah field test with inert anodes.....	35
22a.	pH distribution (0-3 m) for simulation of Paducah field test with iron anodes.	36
22b.	pH distribution (0-0.3 m) for simulation of Paducah field test with iron anodes.	36
22c.	Pore water ion distribution (0-3 m) for simulation of Paducah field test with iron anodes	37
22d.	Pore water ion distribution (0-0.3 m) for simulation of Paducah field test with iron anodes	37
23.	Voltage distribution for simulation of Paducah field test with iron anodes and measured voltages from field test.....	38
24.	Predicted TCE distribution for simulation of Paducah field test with iron anode.	38
25.	Maximum temperature rise vs time	41
26.	Applied voltage vs time	41
27.	Equipotential lines in two-dimensional representation of the pilot test geometry with a buried steel pit	42

List of Tables

	page
Table 1 List of Tasks and Responsible Company	4
Table 2 List of Topical Reports and Responsible Company.....	4
Table 3. Model Parameters	6
Table 4. Parameters Used in Thermal Simulation	12
Table 5. Model Parameters Used in Numerical Simulation of Agar Experiments.	21
Table 6. Model Parameters Used in Numerical Simulation of Paducah Field Experiment.	27

A. Executive Summary

This report summarizes the work conducted in Tasks 2-4, which together make up the Electrokinetic Modeling carried out in this project. The modeling was divided into three main sections: thermal analysis, chemical species transport, and electrode geometry and soil heterogeneity issues. The thermal modeling consisted of development of the governing equations to incorporate Joule heating associated with electroosmosis, heat conduction and convection, and temperature dependencies of electrical conductivity and electroosmotic permeability. These equations were applied to two- and three-dimensional domains that represented hypothetical sites and the actual Paducah pilot site. The model, which was validated with data obtained in the pilot test, shows that constant applied current should lead to a relatively constant flow rate and decreasing power consumption, whereas constant voltage will lead to increasing electroosmotic flow and increasing power consumption. Commonly used electric fields in laboratory experiments of about 100 Vm^{-1} will cause excessive heating in field-scale applications. A nominal electric field of 40 Vm^{-1} (total current was 40 A or 2 A/m^2) in the pilot test resulted in a maximum temperature, both measured and predicted, of 45°C at 10 foot depth. The nominal current density for a larger site made up of $15\text{-m} \times 15\text{-m} \times 12\text{-m}$ -deep zones should be between $0.6\text{-}0.84 \text{ A/m}^2$ to prevent overheating. One conclusion from this analysis is that the Phase 2 test could take at least one year with treatment zones spaced 1 m apart. The economics may favor longer remediation times, and it must be determined if we want to operate at an economic optimum or finish in some predetermined time frame. One possible compromise is to install treatment zones at various spacings in the same test, some to prove effectiveness, and others to prove economics.

To model the transport of chemical species in the LasagnaTM process, a one-dimensional model was developed. This model is based on previous models, but includes additional mechanisms to account for charge transfer in the double layer, pH buffering of the soil, and zeta potential dependency on pH and ionic strength. The model assumes that species can be in one of three layers: the neutral bulk solution, the electrically charged double layer, or adsorbed to the soil surface. Selective partitioning of ions between the soil surface and double layer lead to the zeta potential dependency on pH and ionic strength. The model has been validated with laboratory experiments on agar gels and with results from the Paducah pilot test. The model accurately predicts the migration of low and high pH fronts from electrodes, the effects of iron anodes on reducing the pH drop in the anolyte, and the uniform electric field observed in the pilot test. The model predicts that most of the current is carried in the double layer in the Paducah soil. While this result could not be directly verified in the Paducah field test, the implications of field uniformity and small changes in overall resistivity are consistent with the models predictions.

The results of this model and the corroboration by experimental measurements support some key assumptions made in the thermal model. Specifically, in the thermal model, chemical species transport was neglected. Therefore, redistribution of ions leading to nonuniformities in Joule heating was not accounted for. With the uniform electric field predicted by the model, this assumption appears to be valid. The buffering capacity evidently confines regions of high ionic strength near the electrodes, and the current transport in the double layer prevents low conductivity regions from dominating the overall system.

An analysis was also conducted to compare the use of cylindrical electrodes to the plate geometry used in Phase 1. In summary, cylindrical electrodes may be appropriate for anodes, because they do not intercept the flow. If used as cathodes, a planar treatment zone in their vicinity would probably be required. The cylindrical electrodes can operate at reasonable current densities without boiling water. Because the hottest region is at the electrode, cooling schemes could be used to operate at higher current densities. If iron anodes are used, they will have to be quite massive, and may not be economical

TM Lasagna is a trademark of the Monsanto Company

compared to planar panels. However, anodes made of inert materials may be small and inexpensive to install.

An example of soil heterogeneity was investigated when it was discovered that a steel pit was buried in the vicinity of the pilot test. The results of the analysis indicated that the pit has little effect on the electric field between the electrodes, even given the worst case scenario assumed in the calculations. There is some distortion of the field near the pit, but its effects on the test zone between the electrodes are minimal. The only significant effect is that the current drawn in the case with the pit is about 6% higher than with no pit

B. Background

Statement of the Problem

Contamination in low permeability soils poses a significant technical challenge to in situ remediation efforts. Poor accessibility to the contaminants and difficulty in delivery of treatment reagents have rendered existing in situ treatments such as bioremediation, vapor extraction, and pump and treat, rather ineffective when applied to low permeability soils present at many contaminated sites.

The Solution

The proposed technology combines electro-osmosis with treatment zones that are installed directly in the contaminated soils to form an integrated in situ remedial process. Electro-osmosis is an old civil engineering technique and is well known for its effectiveness in moving water uniformly through low-permeability soils with very low power consumption.

Conceptually, the integrated technology could treat organic and inorganic contamination, as well as mixed wastes. Once developed, the technology will have tremendous benefits over existing ones in many aspects including environmental impacts, cost effectiveness, waste generation, treatment flexibility, and breadth of applications.

Consortium Description

A consortium has been formed consisting of Monsanto, E. I. du Pont de Nemours & Co., Inc. (DuPont) and General Electric (GE), with participation from the Environmental Protection Agency (EPA) Office of Research and Development and the Department of Energy (DOE) Environmental Management Office of Science and Technology. The five members of this group are leaders in their represented technologies and hold significant patents and intellectual property which, in concert, may form an integrated solution for soil treatment. The Consortium's activities are being facilitated by Clean Sites, Inc., under a Cooperative Agreement with EPA's Technology Innovation Office. A schematic diagram of the government/industry consortium is shown on the front page of this topical report.

Management Plan

A Management Plan for this project was prepared by Monsanto and submitted on November 30, 1994. That plan summarized the work plan which was developed in conjunction with DuPont, GE, EPA's Risk Reduction Engineering Laboratory (RREL), Martin Marietta Energy Systems (MMES), and the Department of Energy. The DOE Gaseous Diffusion Plant in Paducah, Kentucky, has been chosen as the site for the initial field tests.

CDM Federal Programs Corporation was chosen to provide the on-site support of the field tests which were installed at the DOE site in November 1994. This experiment tested the combination of electro-osmosis and in situ sorption in the treatment zones. In 1994 and 1995, technology development was carried out under the present contract by Monsanto, DuPont, and GE. These studies evaluated various degradation processes and their integration into the overall treatment scheme at bench and pilot scales.

Technical Deliverables

Tables 1 and 2 summarize the 13 technical tasks and the 8 topical reports that will be written describing the results obtained in the technical tasks. These two tables show which organization is primarily responsible for the tasks and for preparing the topical reports. The present topical report summarizes Tasks No. 2-4—collectively entitled “Electrokinetic Modeling.”

Table 1. List of Tasks and Responsible Company

Task	Company
Task 1 - Evaluation of Treatment Zone Formation Options (5.1.2)	DuPont
Task 2 - Electrokinetic Model Validation and Improvement (6.5)	GE
Task 3 - Design Guidance for Field Experiments (6.6)	GE/DuPont
Task 4 - Analysis of Electrode Geometry and Soil Heterogeneity (6.7)	GE/DuPont
Task 5 - Cost Analysis (7)	Monsanto/DuPont
Task 6 - Lab-Scale Development of Microbial Degradation Process (8.1.2)	DuPont
Task 7 - Lab-Scale Electrokinetic and Microbial Degradation (8.1.6)	Monsanto
Task 8 - Lab-Scale Tests of Lasagna Process Using DOE Paducah Soil (8.1.7)	Monsanto
Task 9 - TCE Degradation Using Non-Biological Methods (8.2.1, 8.2.2.2, 8.2.3.2)	GE/Monsanto
Task 10 - Bench- and Pilot-Scale Tests (9.3)	Monsanto
Task 11 - Establish Contamination Conditions Before and After Tests (10.1.2)	DuPont/MMES
Task 12 - Design and Fabrication of Large-Scale Lasagna Process (12.1, 12.2)	Monsanto/DuPont/Nilex
Task 13 - Large-Scale Field Test of Lasagna Process (12.3, 12.4)	Monsanto/CDM

Table 2. List of Topical Reports and Responsible Company

Topical Report	Company
Task 1 - Evaluation of Treatment Zone Formation Options	DuPont
Tasks 2 - 4 Electrokinetic Modeling	GE
Task 5 - Cost Analysis	Monsanto
Task 6 - Laboratory-Scale Microbial Degradation	DuPont
Tasks 7, 8, 10 - Bench- and Pilot-Scale Tests of Lasagna Process	Monsanto
Tasks 9 - TCE Degradation Using Non-Biological Methods	GE
Task 11 - Contamination Analysis, Before and After Treatment	Monsanto
Tasks 12 and 13 - Large-Scale Field Test of Lasagna Process	Monsanto

C. Draft Topical Report for Tasks No. 2-4

1. Thermal Model

Most laboratory experiments on electrokinetic remediation are conducted under nearly isothermal conditions. However, in field-scale applications, thermal effects can be significant. The temperature of the soil is expected to rise because of Joule heating (I^2R) effects. Under steady-state conditions, the energy supplied to the soil by Joule heating is balanced by thermal conduction of the energy to the boundaries of the soil system. As the size of the treated soil increases, the surface area-to-volume ratio decreases, and the characteristic length for heat conduction increases thus leading to a maximum steady-state temperature rise in the soil that varies with the square of the characteristic length of the region. Therefore, field experiments, which may easily be a factor of ten larger than laboratory experiments, might be expected to have temperature rises on the order of 100-fold larger than the similar laboratory experiment. This estimate assumes that the same electric field is used in both cases. In practice, a steady-state condition in the field may take longer to reach than the remediation itself. To aid in the prediction of the transient thermal behavior, a computer model is developed, and several cases are simulated. The model is verified by comparing its prediction with field data from a pilot test on using electro-osmosis to remediation soil contaminated with trichloroethylene (TCE).

The coupled equations describing the electric and temperature fields are

$$\text{Charge conservation: } \nabla \cdot \sigma(T) \nabla \phi = 0 \quad (1)$$

Combined electroosmotic and hydraulic flow

$$\text{through porous media: } u = -\frac{k_e(T)}{n} \nabla \phi - \frac{k_h(T)}{n} \nabla p \quad (2)$$

$$\text{Energy conservation: } \frac{\partial T}{\partial t} = \frac{k}{\rho c} \nabla^2 T - nu \frac{\rho_w c_w}{\rho c} \cdot \nabla T + \frac{\sigma(T)}{\rho c} \|\nabla \phi\|^2 \quad (3)$$

where ϕ is the electric potential, σ the electrical conductivity, T the soil temperature, ρ the soil density, c the specific heat of the soil, ρ_w the pore water density, c_w the pore water specific heat, n the soil porosity, k the thermal conductivity, and u the pore fluid velocity. Equation 1 makes several simplifying assumptions regarding charge transport in the soil. First, there are no capacitive effects, which should be the case with a dc electric field. Second, charge is transferred predominantly by ionic migration, so that convection in the charged double layer at the soil particle/ pore liquid interface and current carried by diffusion of ions is negligible. And third, the electrical conductivity, to first order, is only a function of temperature. Several investigators¹⁻⁵ have examined the transport of ions in electrokinetic applications, both experimentally and theoretically, and have shown that electrical conductivity becomes a strong function of position as ions get redistributed by the electric field and electrode reactions. However, in soils with moderate buffering capacity it is shown below that this effect can be neglected in certain cases, including the pilot test considered in this work.

Because both fluid viscosity and electrical conductivity are very sensitive to temperature, their temperature dependence has been incorporated in this model. The viscosity dependence is reflected by the electroosmotic permeability, k_e , which varies inversely with viscosity, according to the Helmholtz-Smoluchowski equation⁶. That is, the effects of temperature on the zeta potential, dielectric constant, and

solubility of species are ignored. The following expression was used⁷ to relate the temperature dependence of the electroosmotic permeability to the fluid (water) viscosity:

$$\log_{10}\left(\frac{k_e(T)}{k_e(20^\circ\text{C})}\right) = -\log\left(\frac{\mu(T)}{\mu(20^\circ\text{C})}\right) = \frac{1.3273(T - 20^\circ\text{C}) + 0.001053(T - 20^\circ\text{C})^2}{(T - 20^\circ\text{C}) + 125} \quad (4)$$

Laboratory experiments determined that the temperature dependence of soil electrical conductivity can also be expressed as a function of fluid viscosity. The measured conductivity is plotted against temperature in Fig. 1, along with water viscosity calculated using Eq. 4. The observed inverse relation between electrical conductivity and fluid viscosity is consistent with the behavior of ionic aqueous solutions⁸. Thus the temperature dependence of conductivity was also expressed in terms of fluid viscosity as

$$\sigma(T) = \sigma(20^\circ\text{C}) \frac{\mu(20^\circ\text{C})}{\mu(T)} \quad (5)$$

The two-dimensional geometry used in this analysis, and representing the geometry for the field test, is shown in Fig. 2. In this representation, a gravel overburden 1.2 m thick lies above the clay soil. While the overburden is assumed to be saturated and to conduct current, electro-osmosis in this region is neglected because of its high hydraulic permeability. The electrode represents the plate-shaped electrodes used in the field test. The thermal boundary conditions are constant temperature of 15°C at the soil surface and at the domain bottom where groundwater flow is assumed to maintain a constant temperature. The electrical boundary conditions are $\phi(\text{cathode})=0$ and for constant applied voltage $\phi(\text{anode})=\phi_0$. For constant current simulations, the anode boundary condition is $\int_{\text{anode edge}} i dA = I_0$. The parameters used in the exam-

ple computer simulation are given in Table 3. Parameters related to soil properties, with the exception of thermal conductivity, were determined from laboratory tests conducted by Monsanto. The soil thermal conductivity was the only property chosen to yield good agreement between the model and the pilot test data.

Table 3. Model Parameters

Parameter	Value
porosity, n	0.4
thermal conductivity, k	3 W m ⁻¹ K ⁻¹
electrical conductivity, $\sigma_0(20^\circ\text{C})$	0.024 S m ⁻¹
Pore fluid viscosity, $\mu(20^\circ\text{C})$	0.001 kg m ⁻¹ s ⁻¹
soil density, ρ	1970 kg m ⁻³
soil heat capacity, c	1870 J kg ⁻¹ K ⁻¹
water density, ρ_w	1000 kg m ⁻³
water heat capacity, c_w	4180 J kg ⁻¹ K ⁻¹
electroosmotic permeability, $k_e(20^\circ\text{C})$	1·10 ⁻⁹ m ² V ⁻¹ s ⁻¹

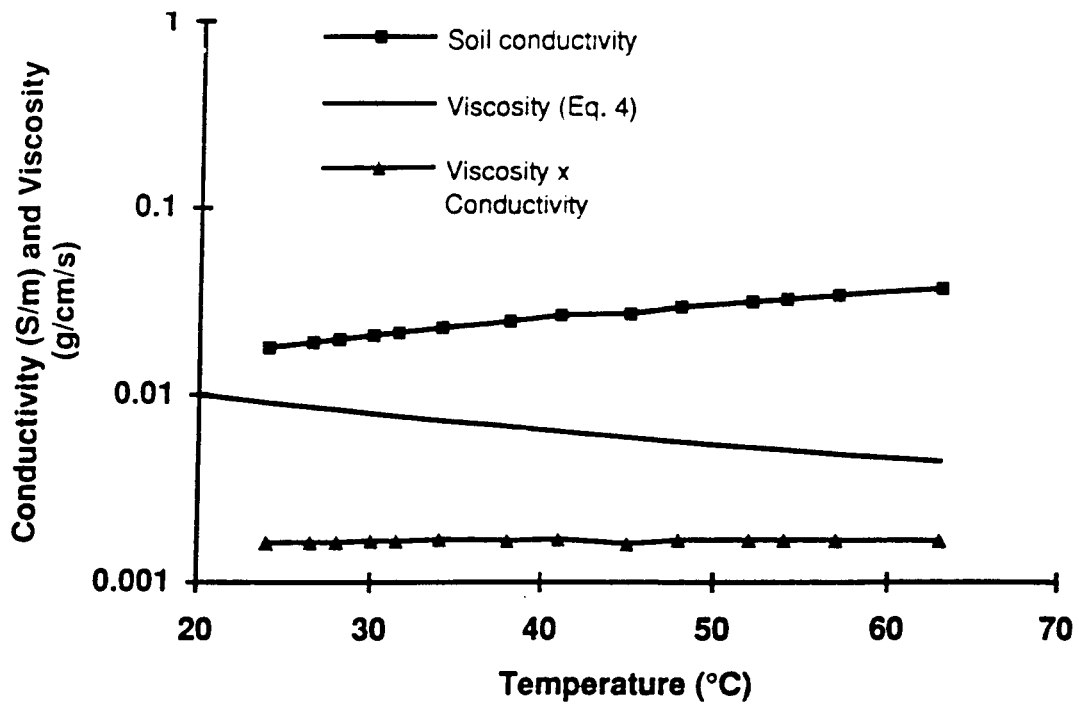


Fig. 1. Comparison of temperature dependence of water viscosity and electrical conductivity of soil (data obtained by D.S. Schultz of DuPont). The product of the two properties is plotted to illustrate their inverse relationship.

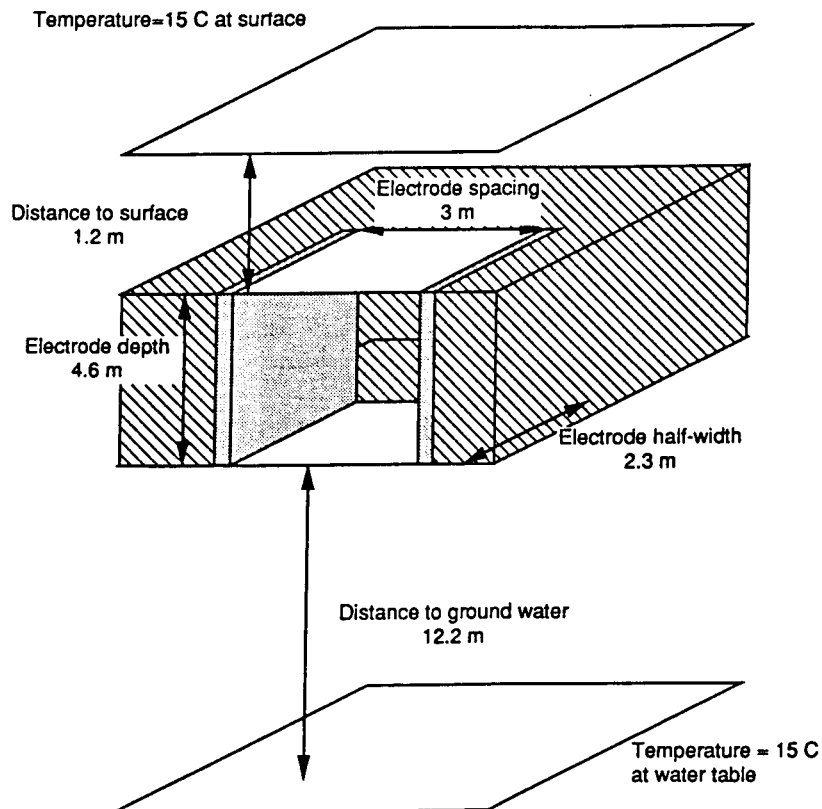


Fig. 2. Geometry for computer simulations.

Three cases are analyzed for maximum soil temperature, power and cumulative energy requirements, and flow rate. In Case (a), a constant current of 6 A per meter of electrode width is applied, which is equivalent to 1.4 A/m² when averaged over the electrode length of 4.24 m. In Case (b), a constant current of 12 A per meter of electrode width, or 2.9 A/m², is applied. In Case (c), the potential was held constant at 135 V, making an applied electric field of 45 V/m. The calculated maximum temperatures for these cases are shown in Fig. 3. For this geometry, the warmest region lies in the center of the domain, and it can be concluded that electroosmotic convection is unimportant in heat transfer, which may not be the case if arrays cylindrical electrodes are used. In such cases, the maximum temperature may occur near the electrodes where the current is concentrated.

From Fig. 3 it can be observed that the temperature rise, in the constant current cases, begins relatively rapidly and then converges toward a steady value. In the constant voltage case, the heating rate increases with time. This behavior can be explained by the fact that the electrical resistivity of the soil decreases with temperature. The power input to the soil, $I^2 R$ or V^2/R , behaves differently for the constant current and constant voltage cases. In the constant current case, the power decreases with time, and in the constant voltage case, the power increases with time, shown in Fig. 4.

The effect of heating on the electroosmotic flow rate is shown in Fig. 5. The pore volumes represented in Fig. 5. refer to one-fifth of the total pore volume between the electrodes, because in the pilot test, four activated carbon treatment zones were installed at equal spacings, parallel to, and between, the electrodes. The linear relation between pore volumes removed and time, for the constant current cases, indicates the cancellation of two effects. As the soil warms, the electrical conductivity increases, resulting in a lower field, or driving force, for electro-osmosis. These calculations show that this effect is balanced by the increase in permeability because of the decrease in pore water viscosity with temperature. In the case of constant voltage, the field is essentially constant, resulting in increased electro-osmosis as the soil warms. This behavior is verified by the pilot test data, which are also plotted in Fig. 5 and coincide with the flow produced by the 1.4 A/m² simulation.

Good agreement is also seen between the model predictions and the pilot test measurements of temperature vs time shown in Fig. 6. The model agrees well with the measured temperatures at a depth of 10 ft, and slightly underpredicts the temperature at a depth of 5 ft. The reason for the discrepancy could be that the soil was represented by a uniform isotropic thermal conductivity, whereas spatially dependent anisotropic properties may be more appropriate. Such complexity was not incorporated in the model, because the simplifications, which were used, seemed to provide the correct estimate of the maximum temperature in the soil.

The model also accurately predicts the transient power consumption plotted in Fig. 7. In estimating the power in the three-dimensional pilot test from a two-dimensional simulation, a correction factor was used to account for the additional fringing current that exists in the three-dimensional case. The correction factor was determined by assuming that the fringing current in the three-dimensional case is the same magnitude, per electrode edge length, as in the two-dimensional case. The fringing current in the two-dimensional case can be determined by comparing the current for one-dimensional and two-dimensional geometries. In one-dimension, the expected current for Case (a) above, which represents the nominal 1.4 A/m² used in the pilot test, would be

$$I = \sigma(T)\Delta V / L_{Area} = 0.021S / m(149V / 3m)5m4.24m = 22.4A.$$

In this example, the electrical conductivity is determined at the initial time when the soil has uniform properties and a temperature of 15°C. The current in the two-dimensional calculation is 6.1A/m width of soil (30.5 A for the 5-m-wide site). Therefore, the fringing current is 30.5 - 22.4 A = 8.1 A. This fringing current occurs predominately through the soil below the depth of the electrodes and is equally distributed along 5-m-electrode width. Hence the fringing current per length is 8.1/5 = 1.6 A/m. In three dimensions it is reasonable to expect the fringing current that leaks around the sides of the test zone, per electrode edge

length, would be about the same as the current that passes beneath the test zone. Since there are an additional 8.48 m (2X vertical electrode dimension) of electrode edges in the actual three-dimensional geometry, compared to the two-dimensional simulation, an additional 8.48 m $1.62\text{ A/m} = 13.7\text{ A}$ would be expected, that is, a total of $30.5 + 13.7 = 44.2\text{ A}$ would be expected. Therefore, the correction factor used in estimating the three-dimensional current from the two-dimensional simulation was $44.2/30.5 = 1.4$.

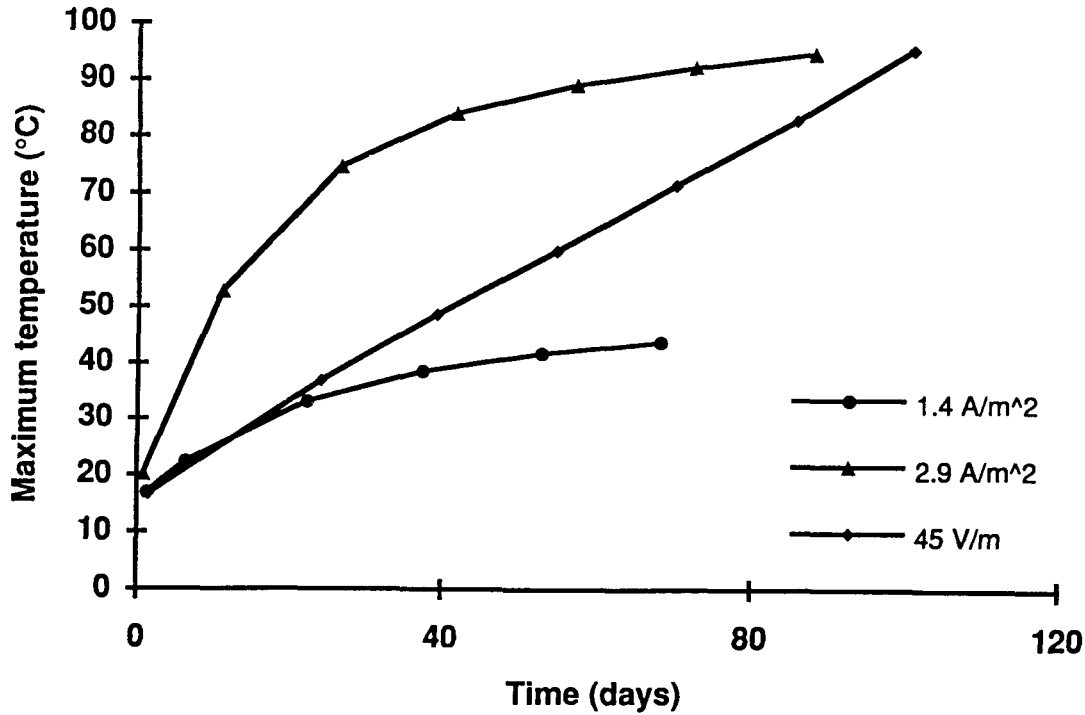


Fig. 3. Maximum temperature vs time for three simulated cases.

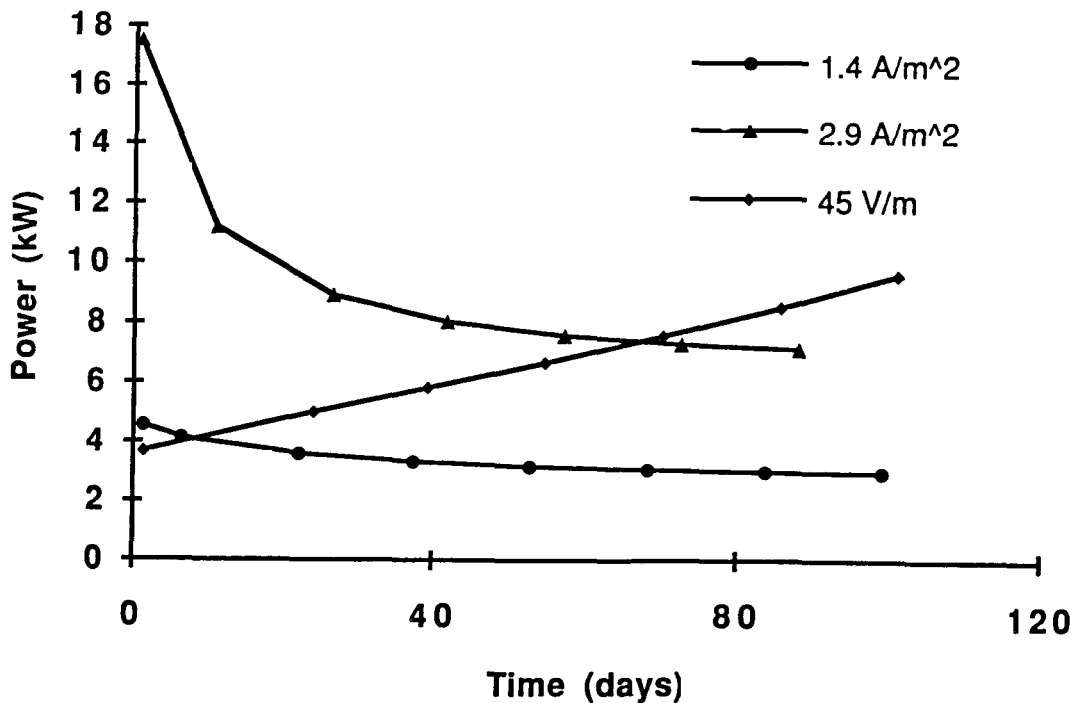


Fig. 4. Power consumption vs time for three simulated cases.

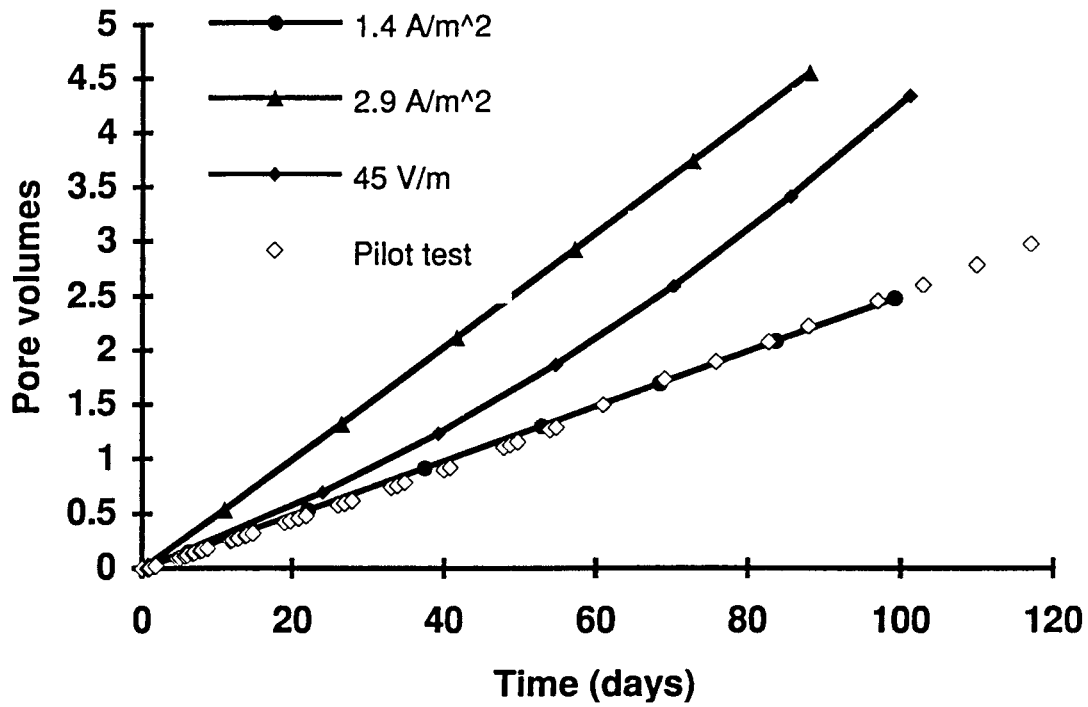


Fig. 5. Pore volume moved through soil. These pore volumes are based on treatment zones spaced at 0.75-m intervals (see text).

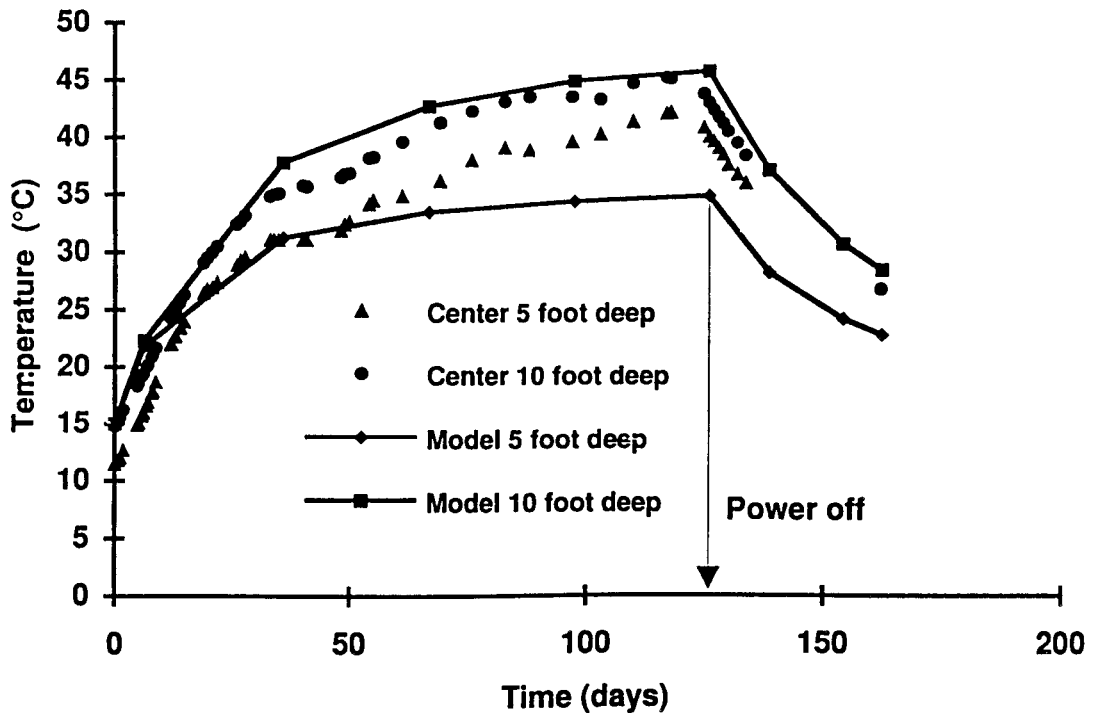


Fig. 6. Comparison of model predictions of temperatures at 5-and 10-ft depths and data from the field test.

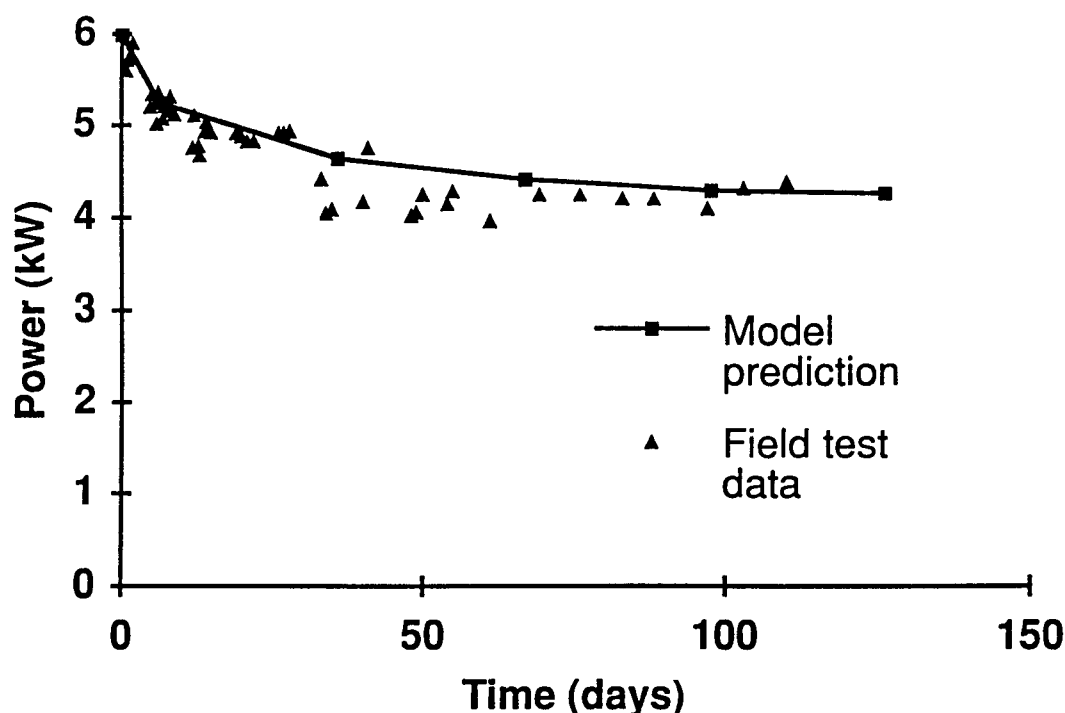


Fig. 7. Comparison of model prediction and field test data of power consumption vs time. Power from 2-D model has been corrected to account for 3-D fringing of current.

In summary, a mathematical model has been developed that accurately predicts the thermal behavior of electrokinetic remediation. The model shows that constant applied current should lead to a relatively constant flow rate and decreasing power consumption, whereas constant voltage will lead to increasing electroosmotic flow and increasing power consumption. While steady-state thermal conditions are not reached in the time scales associated with the pilot test (~100 days), the constant current cases approach their steady-state temperature distribution much sooner than the constant voltage cases. Commonly used electric fields in laboratory experiments of about 100 Vm^{-1} would appear to cause excessive heating in field-scale applications.

Full-Scale Test

The larger size of the Phase 2 site for Lasagna may cause the temperature rise experienced deep in the soil to be larger than that measured in the Phase 1 pilot test. Two-dimensional calculations using FIDAP® (commercial software by Fluid Dynamics International, Evanston, IL) were conducted to evaluate this effect. The geometry used in the model assumed infinitely wide plate electrodes sunk 12 m from the surface and spaced 5 m apart. The thermal boundary conditions were a constant 20°C at the soil surface and at 15-m depth, representing an aquifer. The electrodes were assumed to be part of an infinite array of alternating anodes and cathodes so that heat was not conducted, and current did not flow across the planes containing the electrodes (i.e., symmetry was imposed as a boundary condition at the electrodes). The

imposed symmetry resulted in a nearly one-dimensional temperature profile, with temperature varying only as a function of depth. Therefore, these calculations should be accurate regardless of electrode spacing, so long as the same current density is used. The parameters used in the calculations are shown in Table 4 and were verified by comparison with the pilot test data. The results, as shown in Fig. 8, indicate that a current density of 0.84 A/m^2 will produce a hot spot about 6-7 m deep that will increase nearly 75°C over the course of the process. In Fig. 9, the pore volumes moved through the treatment zones are plotted vs time. In these calculations a pore volume is based on 1-m-treatment zone spacing. For 0.84 A/m^2 , two pore volumes are displaced after about 280 days. Halving the current results in a steady-state temperature rise of about 27°C . Using 0.42 A/m^2 , 580 days are required to move two pore volumes through the treatment zones.

Parameter	Value
Electrical conductivity (20°C)	$0.024 \Omega^{-1} \text{ m}^{-1}$
Thermal conductivity	$3.0 \text{ W m}^{-1} \text{ K}^{-1}$
Electroosmotic permeability (20°C)	$10^{-9} \text{ m}^2 \text{ V}^{-1} \text{ s}^{-1}$
Soil density	1980 kg m^{-3}
Soil heat capacity	$1870 \text{ J kg}^{-1} \text{ K}^{-1}$
Electrode spacing	5 m
Treatment zone spacing	1 m
Electrode depth	12 m

Table 4. Parameters Used in Thermal Simulation.

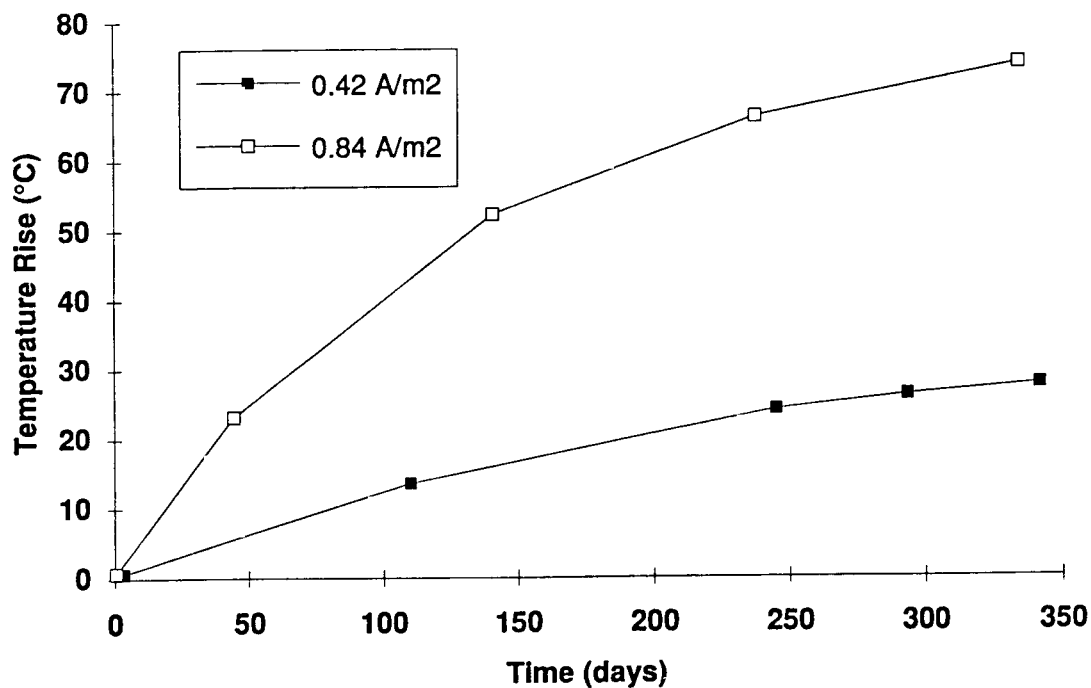


Fig. 8. Maximum temperature rise vs time. Electrodes are 5 m apart and 12 m deep. Depth to 20°C aquifer is 15 m.

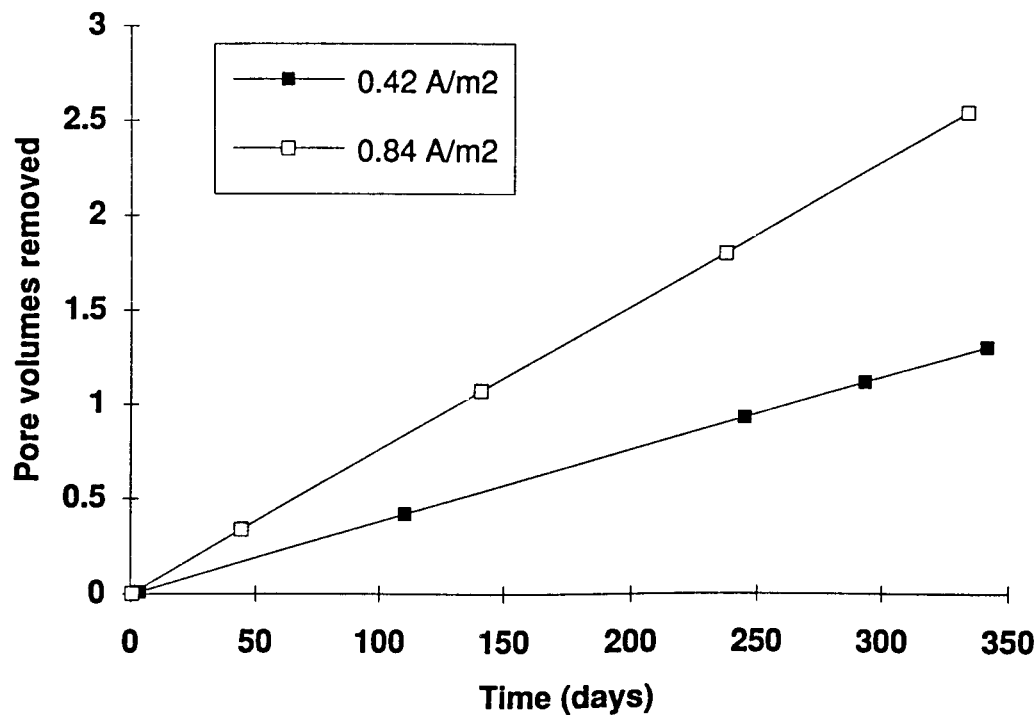


Fig. 9. Pore volumes removed vs time. Electrodes are 5 m apart and 12 m deep. Treatment zones are spaced 1 m apart. Depth to 20°C aquifer is 15 m.

If we assume a moderate current density of 0.6 A/m^2 , the total initial power for a site measuring $15 \text{ m} \times 15 \text{ m} \times 12 \text{ m}$ would be about 40.5 kW ($\text{current density}^2 / \text{conductivity} \times \text{volume} = 0.6^2 / 0.024 \times 2700$). If we assume 0.84 A/m^2 , then the initial power would be 79.4 kW . The power would gradually decrease with time as the conductivity increased with temperature. The degree of decrease in power can be seen in Fig. 10, where the applied voltage is plotted vs time. Because the current is held constant, the power is simply proportional to the voltage.

One conclusion from this analysis is that the phase 2 test could take at least one year with treatment zones spaced 1 m apart. The economics may favor longer remediation times; however, it must be determined if we want to operate at an economic optimum or finish in some predetermined time frame. One possible compromise would be to install treatment zones at various spacings in the same test: closer spaced zones would prove effectiveness, and further spaced zones would verify economics.

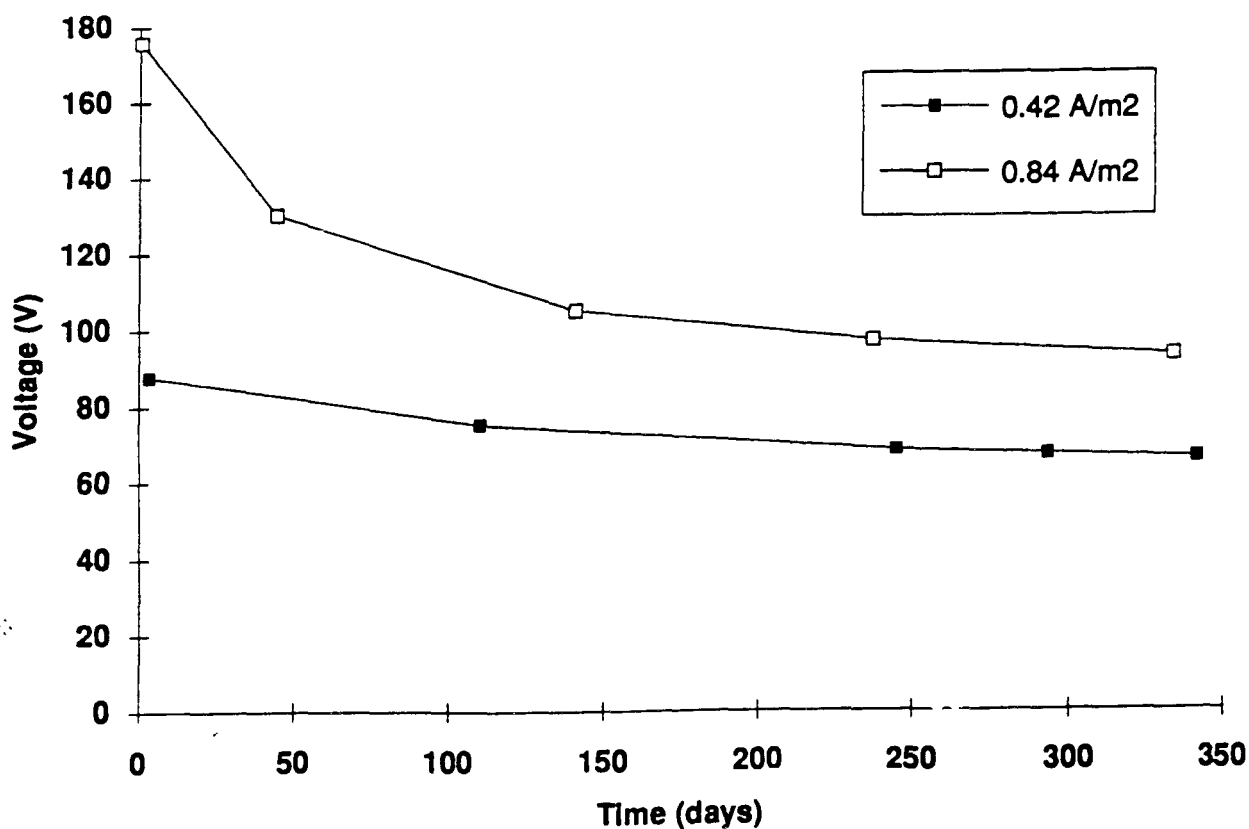


Fig. 10. Applied voltage vs time. Electrodes are 5 m apart and 12 m deep. Depth to 20°C aquifer is 15 m .

2. Chemical Species Model

Modeling of species transport in electrokinetic remediation is necessary to understand and to predict how contaminants will be removed from, and ion redistributed, in the soil. The transport mechanisms of electro-osmosis, ionic migration, electrode reactions, and soil/water chemistry form perhaps the minimum set of processes that must be considered when modeling electrokinetic remediation. Incorporation of all these mechanisms in typical convective-diffusion differential equation models has been undertaken by several authors^{1,2,4}, all of whom make important simplifying assumptions to facilitate computation. For instance, in the earlier models by Shapiro and Acar, the pH buffering capacity of soil was neglected. Recently researchers at MIT have presented^{10,11} work that includes soil buffering based on acid/base titrations of the soil. It was shown that including the soil-buffering capacity was essential to predict the transport of heavy metals and the distribution of the electric field.

Another assumption that has been implicit in the models of electrokinetic remediation is that all transport takes place in the electrically neutral pore solution. That is, transport in the charged double layer is negligible compared to the bulk pore liquid. While this is a valid assumption in soils in which the thickness of the charged double layer is small compared to the soil pore size, in many cases where electro-osmosis is important, this assumption does not apply. For example, in a clay, the pore size, a , may be about $0.1\ \mu\text{m}$, and the double layer thickness, λ , of a groundwater with a 1-mM-electrolyte concentration may be about $0.01\ \mu\text{m}$ ¹², or about 10% of the pore radius. If one approximates the pore as cylindrical, then the fraction of the pore solution in the double layer is about $(2a/\lambda - 1)/(a/\lambda)^2 = 19\%$. When one considers that the concentration of ions in the double layer can be many times that in the pore solution, it is clear that, in this example, the transport of ions in the double layer is significant.

The model developed in this project includes both transport in the double layer and the pH buffering capacity of the soil along with electro-osmosis, ionic migration, electrode reactions, and soil/water chemistry. In addition, a model of the pH and ionic strength dependence of the zeta potential is also included. To incorporate these effects, the following assumptions have been made:

(1) Cation adsorption determines pH buffering capacity, and sodium and ferrous ions represent all cations that can be exchanged with H^+ .

$$H_{ads}^+ + Na_{ads}^+ + 2Fe_{ads}^{+2} = CEC \quad (6)$$

where CEC is the cation exchange capacity, and the subscript ads represents adsorbed species.

(2) H_{ads}^+ is a function of the pore solution pH only and can be determined by titration of soil with strong base and acid.

$$H_{ads}^+ = fnc(H^+) \quad (7)$$

(3) In this model “adsorbed” implies that the species is not in the neutral pore solution. The adsorbed ions are assumed to be partitioned between those adsorbed on soil surface and those dissolved in the double layer.

$$\begin{aligned} H_{ads}^+ &= H_s^+ + H_{dl}^+ \\ Na_{ads}^+ &= Na_s^+ + Na_{dl}^+ \\ Fe_{ads}^{+2} &= Fe_s^{+2} + Fe_{dl}^{+2} \end{aligned} \quad (8)$$

where the subscript s signifies adsorbed on the soil surface and the subscript dl means dissolved in the double layer. In this model, the concentrations of adsorbed species and those in the double layer reflect average concentrations across the pore and are based on pore liquid volumes. Therefore, for example, the

concentration H_s^+ in moles per liter is actually the moles of H^+ adsorbed on the soil per unit surface area, multiplied by the ratio of soil surface area to pore liquid volume.

(4) The partitioning of ions adsorbed to the surface and those in the double layer can be approximated by a linear relation. The divalent ferrous ions are assumed to be completely adsorbed on the soil surface:

$$\begin{aligned} H_s^+ &= f \cdot H_{ads}^+ \\ Na_s^+ &= g \cdot Na_{ads}^+ \\ Fe_s^{+2} &= Fe_{ads}^{+2} \end{aligned} \quad (9)$$

where f and g are adsorption constants between zero and unity.

(5) It is assumed that divalent ferrous ions will be adsorbed preferentially compared to monovalent sodium ions:

$$\text{If } Fe^{+2} > 0, \text{ then } Na_{ads}^+ = 0 \quad (10)$$

Surface Charge and Zeta Potential Relation

The surface charge and zeta potential can be calculated from the ions adsorbed on the soil surface. The difference between the adsorption constants f and g for H^+ and Na^+ leads to the pH dependence of the surface charge, or zeta potential. The average soil surface charge varies linearly with adsorbed cations:

$$\sigma = \sigma_0 + \frac{F1000}{\rho A_s} (H_s^+ + Na_s^+ + 2Fe_s^{+2}) \quad (11)$$

where σ is the surface charge density in C/m², σ_0 an empirical constant, F Faraday's constant (96500 C/mol), ρ the soil density, and A_s the specific surface area of the soil (in m⁻¹). Combining Eqs. 9 and 11:

$$\sigma = \sigma_0 + \frac{F1000}{\rho A_s} (fH_{ads}^+ + gNa_{ads}^+ + 2Fe_{ads}^{+2}) \quad (12)$$

Combining the assumption of constant CEC (Eq. 6) and Eq. 12 gives

$$\sigma = \sigma_0 + \frac{F1000}{\rho A_s} ((f - g)H_{ads}^+ + gCEC + 2Fe_{ads}^{+2}) \quad (13)$$

Because H_{ads}^+ is assumed to be only a function of pore solution pH, it is specified once the pore solution pH is known. The H_{ads}^+ vs pH relation can be determined experimentally by titration of a known mass of soil with strong acid and base. An example of this relation is shown for the Paducah soil used in the Phase 1 Lasagna test.

The concentration of H_{ads}^+ in terms of moles H^+ adsorbed per volume of pore liquid in a soil with a specific gravity of 2 and a porosity of 0.4 is shown in Fig. 11. A fourth order polynomial is used to fit the data and to define the function in Eq. 7 ($H_{ads}^+ = fnc(H^+)$). With this function and the soil properties ρ and A_s known, the surface charge model constants, f , g , and σ_0 , must be determined to calculate the surface charge σ using Eq. 13. These constants are evaluated by applying some experimentally determined constraints. One set of constraints that has been used to evaluate f , g , and σ_0 is

- (1) the surface charge density or zeta potential of the soil is known at a particular pH and ionic strength
- (2) the pH of zero charge is known
- (3) the electrical conductivity of the soil at a particular pH and ionic strength is known

These three constraints fully specify the model parameters. Application of the first two constraints is straightforward. Applying the electrical conductivity constraint requires an additional equation to relate soil conductivity to concentration of adsorbed ions. In the model developed here, the soil conductivity is a combination of the conductivity of the pore solution and the conductivity of the ions in the double layer. The third layer of ions adsorbed to the surface does not contribute to the electrical conductivity. Hence

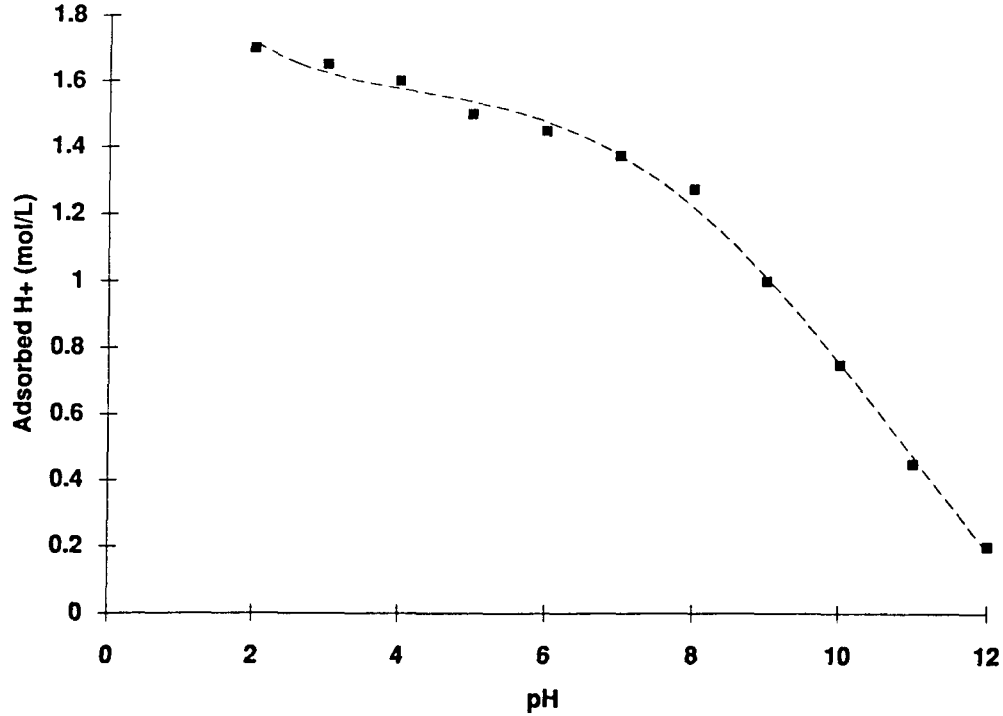


Figure 11. Adsorbed H⁺ concentration (based on pore water volume) vs pH determined from titration data, assuming a soil density of 2 g/cc and porosity of 0.4.

$$\begin{aligned}\sigma_{soil} &= \frac{n}{\tau^2} (\sigma_{solution} + \sigma_{dl}) \\ &= \frac{n}{\tau^2} F^2 \left(\sum z_i^2 v_i c_i + (1-f) v_{H^+} H_{ads}^+ + (1-g) v_{Na^+} Na_{ads}^+ \right)\end{aligned}\quad (14)$$

where a capillary model of the porous soil is used¹ in which n is the porosity, and τ is the tortuosity of the soil. c_i is the molar concentration of species i in the pore solution outside the double layer, z_i is the charge number of species i in solution, and v_i is the mobility of species i ($v_i = D_i/RT$ using the Nernst-Einstein relation). In this model, only H⁺ and Na⁺ in the double layer are considered. Counter ions such as OH⁻ and Cl⁻ are probably at much lower concentrations and are therefore neglected.

The zeta potential is approximated by the following:

$$\zeta = \sigma \frac{\lambda}{\epsilon} \quad (15)$$

where ζ is the zeta potential (V), λ is the Debye length (m), and ϵ is the electrical permittivity of the pore water (F/m). The Debye length is based on the concentration of dissolved ions in the pore fluid and is given by

$$\lambda = \sqrt{\frac{\epsilon RT}{F^2 \sum_i z_i^2 c_i}} \quad (16)$$

Application of the three layer model to the Paducah soil is illustrated in Fig. 12. The model predicts ζ as a function of pH and ionic strength (via the double layer thickness).

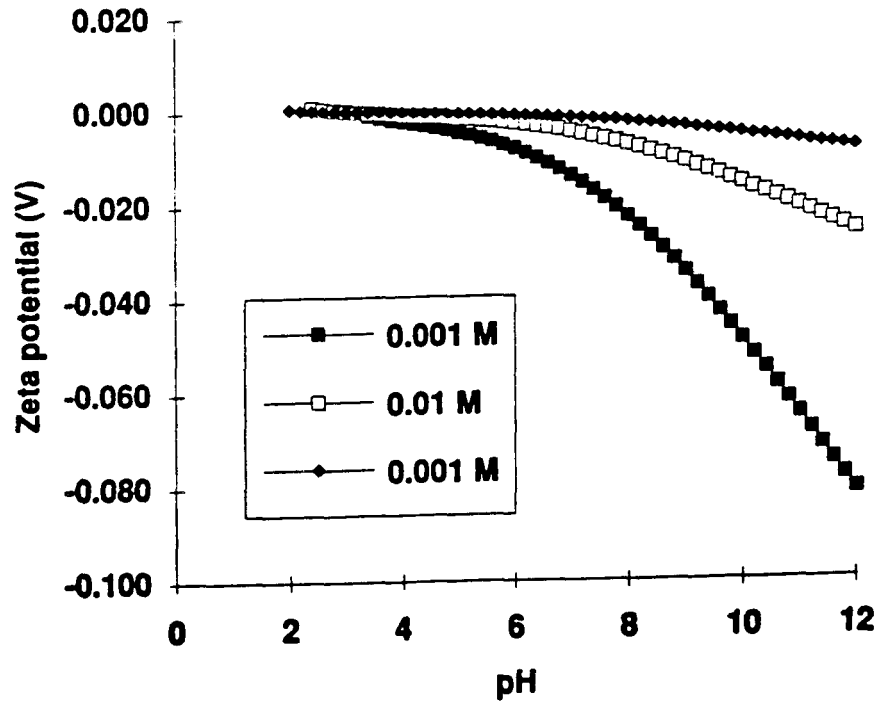


Figure 12. Application of the model to Paducah soil. The soil properties are $\rho = 2000 \text{ kg/m}^3$, $A_s = 3 \times 10^5 \text{ m}^2/\text{m}^3$. The constraints used to evaluate the model parameters are (i) $\zeta = 5.6 \text{ mV}$ at $\text{pH} = 7$ and ionic strength = 6 mM, (ii) the point of zero charge is $\text{pH} = 3.1$, and (iii) the electrical conductivity of the soil is $0.042 \text{ } \Omega^{-1}\text{m}^{-1}$. The resulting parameters are $f = 0.998$, $g = 0.98$, and $\sigma_0 = -0.273 \text{ Cm}^{-1}$.

Transport Model

The transport of the species dissolved in the pore water is governed by the convective-diffusion equation:

$$\frac{\partial c_i}{\partial t} = D_i \frac{\partial^2 c_i}{\partial x^2} - \frac{\partial}{\partial x}(u_i c_i) + R_i \quad (17)$$

where c_i is the concentration of species i in units of moles per liter of pore water, D_i is the effective diffusion coefficient (accounting for soil structure) of species i , and u_i is the velocity of species i which is a combination of convection resulting from electro-osmosis and electromigration of charged species. R_i is a reaction rate (moles/liter/second) that can represent association/dissociation reactions in the aqueous phase and reactions that involve transfer of species between adsorbed and dissolved phases. The development and the application of this model have been described in detail^{1,9,13}. It is important to note that the species velocity, u_i , consists both of electroosmotic and ionic migration components. For species in the double layer, it is assumed that the diffusivity and ion mobility are the same as if the species were in the neutral pore solution. However, the electroosmotic convection of species in the double layer is assumed to be one-half the bulk fluid velocity. The factor of 1/2 reflects, at least qualitatively, the average velocity profile in the double layer.

In this application of the model, 12 species are considered: Na^+ , Na^+_{s} , Na^+_{dl} , Cl^- , H^+ , H^+_{s} , H^+_{dl} , OH^- , Fe^{+2} , $\text{Fe}(\text{OH})_2$, $\text{Fe}^{+2}_{\text{s}}$, and TCE. Chemical equilibria in neutral pore liquid provide three constraints:

$$\begin{aligned} H^+ OH^- &= 10^{-14} \\ Fe^{+2} / (H^+)^2 &= 10^{13.3} \\ Na^+ + H^+ + 2Fe^{+2} - Cl^- - OH^- &= 0 \end{aligned} \quad (18)$$

The first expression in Eq. 18 describes the dissociation of water, the second describes the solubility of $\text{Fe}(\text{OH})_2$, and the third expression enforces electroneutrality in the neutral pore fluid.

The partitioning of adsorbed species between the soil surface and the double layer provides three additional constraints as shown in Eq. 9. Equations 6 and 7 also constrain the transport of the 12 species, providing a total of 8 soil/water equilibrium constraints. Hence, the number of independent species transport equations of the type of Eq. 17 is $12 - 8 = 4$. Using the method of eliminating the reaction terms in Eq. 17 described in references [9],[10], and [12], it is convenient to solve the convective-diffusion equations for the following conserved quantities: TCE, $H_{\text{total}} = H^+ + H^+_{\text{s}} + H^+_{\text{dl}}$, Cl^- , $\text{Fe}_{\text{total}} = \text{Fe}^{+2} + \text{Fe}^{+2}_{\text{s}} + \text{Fe}(\text{OH})_2$. The velocities and diffusivities of Na_{total} and Fe_{total} are based on weighted averages of the component species. Species adsorbed on the soil surface and $\text{Fe}(\text{OH})_2$ precipitate do not contribute to convective or diffusive transport. As described above, species in the double layer (Na^+_{dl} and H^+_{dl}) have ion migration velocities identical to their adjacent species in the neutral pore fluid, and have electroosmotic velocities of one-half the pore fluid.

Charge Transport

Current transport is given by

$$i = -\sigma(x) \frac{\partial \phi}{\partial x} - F \sum_i z_i D_i \frac{\partial c_i}{\partial x} + F \frac{u_{eo}}{2} \sum_i z_i c_{i,dl} \quad (19)$$

where σ is the soil conductivity (pore fluid and double layer contributions), ϕ is the electric potential, and u_{eo} the electroosmotic velocity. The last term pertaining to the convective transport of current reflects the fact that convection in the charged double layer carries current, as opposed to the neutral pore solution. Of the 12 species accounted for in this application of the model, 7 (Na^+ , Na_{dl}^+ , Cl^- , H^+ , H_{dl}^+ , OH^- , Fe^{+2}) are involved in charge transport. In this one-dimensional model, because the soil/water system is electrically neutral, the current is independent of position, although it may change with time, depending on the boundary conditions. Given the species concentration fields at the beginning of a time step, Eq. 19 can be integrated to yield the local electric field, which in turn, determines electroosmotic and local ionic velocities.

Solution Procedure

A finite element code was used to integrate the four convective-diffusion equations for TCE, H_{total} , Cl^- , and Fe_{total} . Having determined the incremental changes in these species, the 8 soil/water equilibrium constraints were used to determine the distribution of the 12 species. Then Eq. 19 was used to calculate the local electric field, so that the velocities for the next time step could be determined. As reported by Jacobs et al., it was found in this work that artificial diffusion enabled larger time steps (on the order of 10 s). The global Peclet, $u_{eo}L/D$, number for these simulations was on the order of 10^3 , therefore increasing the diffusivity (not the ionic mobility, however) by a factor of 10 does not significantly reduce accuracy since convection will still dominate.

Example Simulations

The chemical species transport model was run for four scenarios. The first two cases were chosen to verify the predictions of the model with laboratory tests conducted on agar gels. The model simulated two agar experiments, one using an inert platinum anode, and the other using an iron electrode. Agar was used instead of soil because it was easy to add pH indicating dyes to the pore solutions, so that the migration of pH fronts could be monitored. The second two cases were simulations of the Paducah field test in which the electrode were 3 m apart. Both inert anode and iron anodes were analyzed in the pilot test geometry.

Agar experiments

The parameters used in the modeling of the agar experiments are listed in Table 5. The buffering capacity of the agar gel was measured by titration of HCl and NaOH into a solution of 0.9% (wt) agar in distilled water and by converting the capacity to reflect the 2% solution used in the experiments. The amount of H^+ adsorbed per unit volume of gel is plotted in Fig. 13. The fourth order curve to fit the titration data was

$$c_{\text{H}^+}^{\text{ads}} = -3.633 \cdot 10^{-3} + 1.021 \cdot 10^{-2} \text{pH} - 4.514 \cdot 10^{-3} \text{pH}^2 + 7.251 \cdot 10^{-4} \text{pH}^3 - 3.985 \cdot 10^{-5} \text{pH}^4 \quad (20)$$

The curve was truncated at low pH, so that for $\text{pH} < 2.4$ $c_{\text{H}^+}^{\text{ads}} = 0.0034 \text{ M}$, thus reflecting the fact that there is a limited buffering capacity for H^+ , which the pH range covered in the titration did not resolve.

Table 5. Model Parameters Used in Numerical Simulation of Agar Experiments.

Property	Variable	Value
porosity	n	1.0
tortuosity	τ	1.0
Diffusivity of TCE, m^2s^{-1}	D_1	$1.0 \cdot 10^{-9}$
Diffusivity of Na^+ , m^2s^{-1}	D_2	$1.3 \cdot 10^{-9}$
Diffusivity of Cl^- , m^2s^{-1}	D_3	$2.0 \cdot 10^{-9}$
Diffusivity of H^+ , m^2s^{-1}	D_4	$9.4 \cdot 10^{-9}$
Diffusivity of OH^- , m^2s^{-1}	D_5	$5.3 \cdot 10^{-9}$
Diffusivity of Fe^{+2} , m^2s^{-1}	D_8	$0.72 \cdot 10^{-9}$
Permittivity of water, Fm^{-1}	ϵ	$7.0 \cdot 10^{-9}$
Viscosity of water, $\text{kgm}^{-1}\text{s}^{-1}$	μ	$1.0 \cdot 10^{-3}$
Agar density, kg m^{-3}	ρ	$1.0 \cdot 10^{+3}$
Specific surface area, m^2kg^{-1}	A_s	$1.0 \cdot 10^{-5}$
Fraction adsorbed H^+ on soil surface	f	0.998
Fraction adsorbed Na^+ on soil surface	g	0.98
Initial NaCl concentration, molL^{-1}	c_2, c_3	$1.25 \cdot 10^{-2}$
Concentration of H^+ exchange sites, molL^{-1}	cec	$3.4 \cdot 10^{-3}$
Surface charge constant, Cm^2	σ_0	$-1.43 \cdot 10^{-3}$
Electrode spacing, m	L	$1.3 \cdot 10^{-2}$

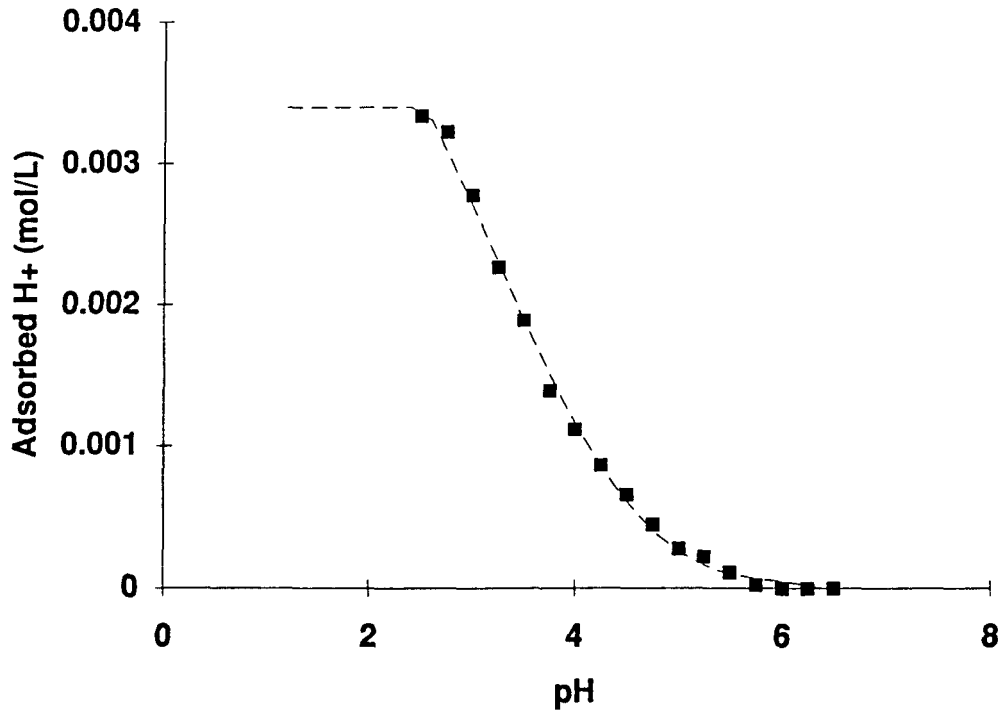
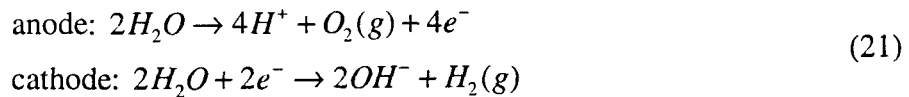


Figure 13. Titration curve for 2% solution of agar gel.

The results of the model simulation of the agar experiment using the platinum anode are shown in Figs. 14.a-d. Figure 14a shows the propagation of a low pH front from the anode and a high pH front from the cathode. These fronts result from the electrode reactions that for inert electrodes are



The pore water ions, which are represented by sodium and chloride, get redistributed as shown in Fig. 14b. Chloride ions become concentrated at the anode, producing the low pH conditions, while sodium ions accumulate at the cathode and raise the solution pH. Sodium ions are also released from the agar as part of the buffering reactions (Eq.6). The predicted voltage distribution is shown in Fig. 14c. In these simulations, the applied electric boundary conditions are an imposed current that was specified to match the transient applied current in the laboratory experiments. In the experiments, a constant potential was applied to the electrodes; however, because significant voltage drops occurred between the electrodes and the agar surfaces, the effective applied voltage was not constant. A comparison of the predicted and measured electric fields for both agar experiments is shown in Fig. 15a-b. It is evident from these curves that the model predicts the trends in the voltage response when an applied current is imposed as a boundary condition.

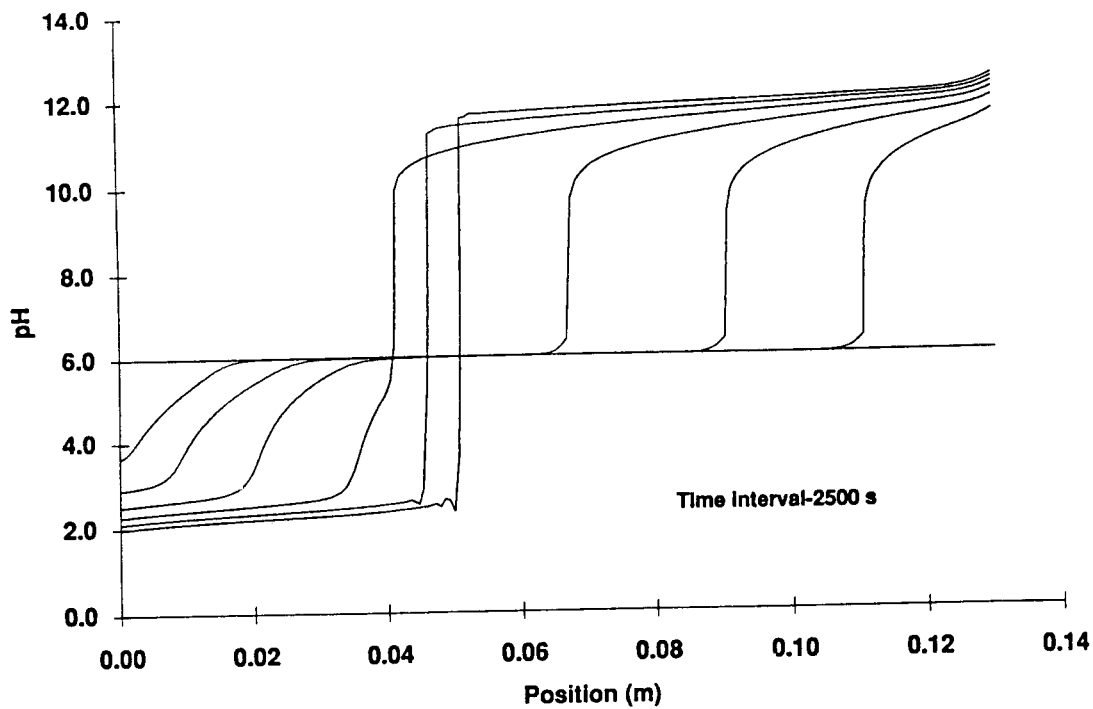


Figure 14a. pH distribution for agar simulation with inert anode. Model parameters are listed in Table 5.

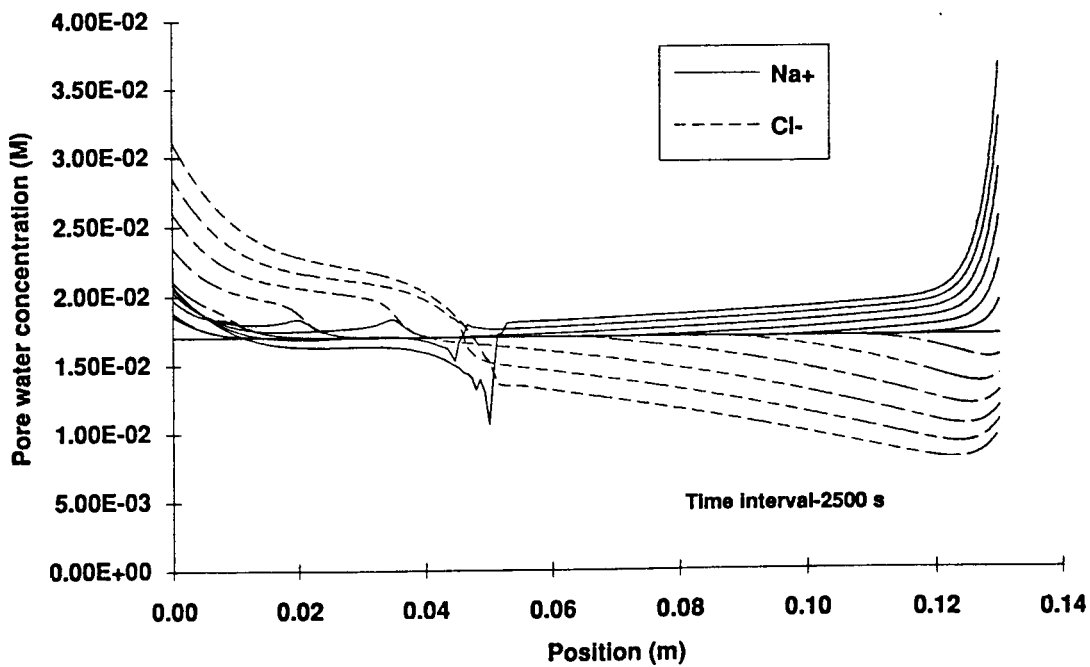


Figure 14b. Pore water ion distribution for agar simulation with inert anode. Model parameters are listed in Table 5.

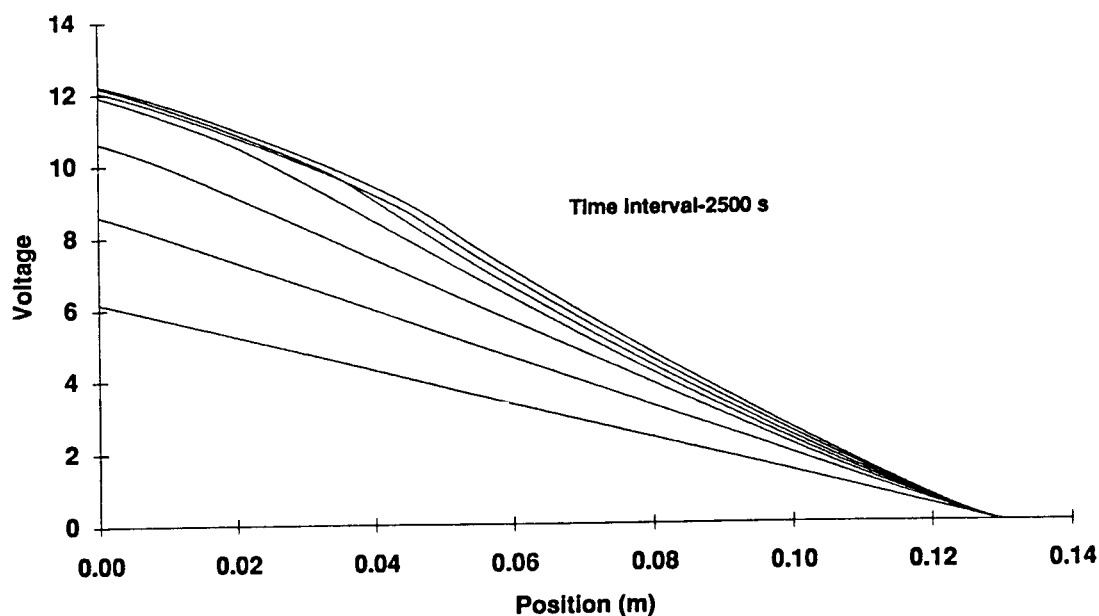


Figure 14c. Voltage profile for agar simulation with inert anode. Model parameters are listed in Table 5.

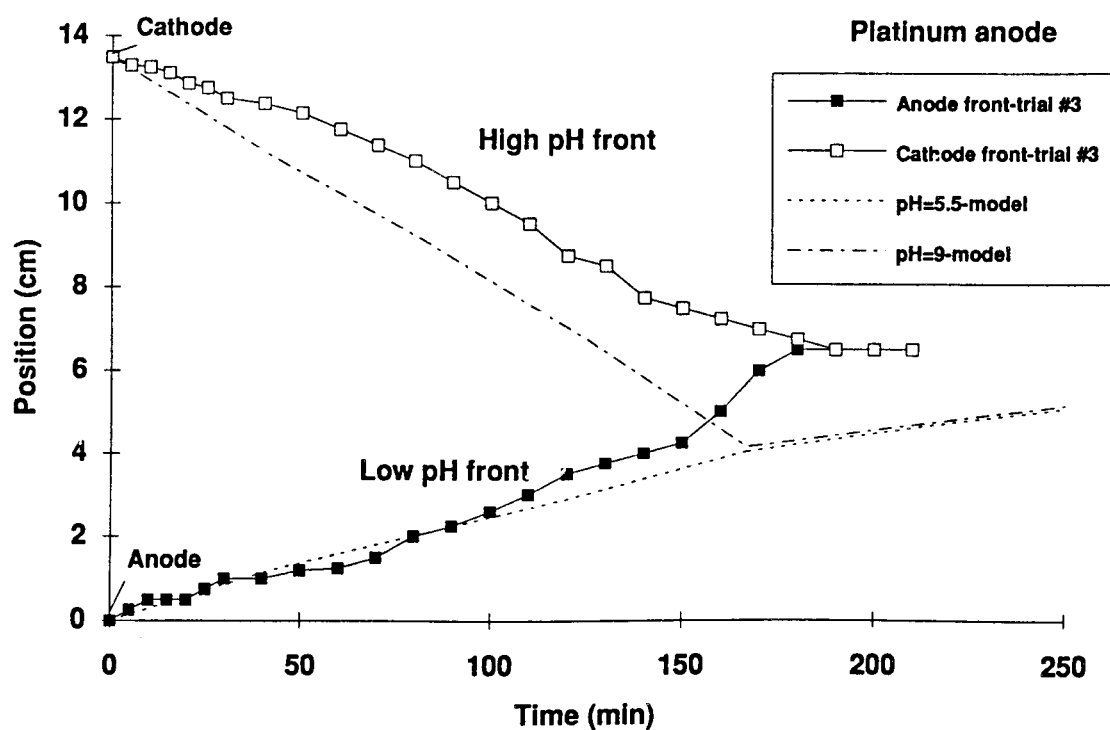
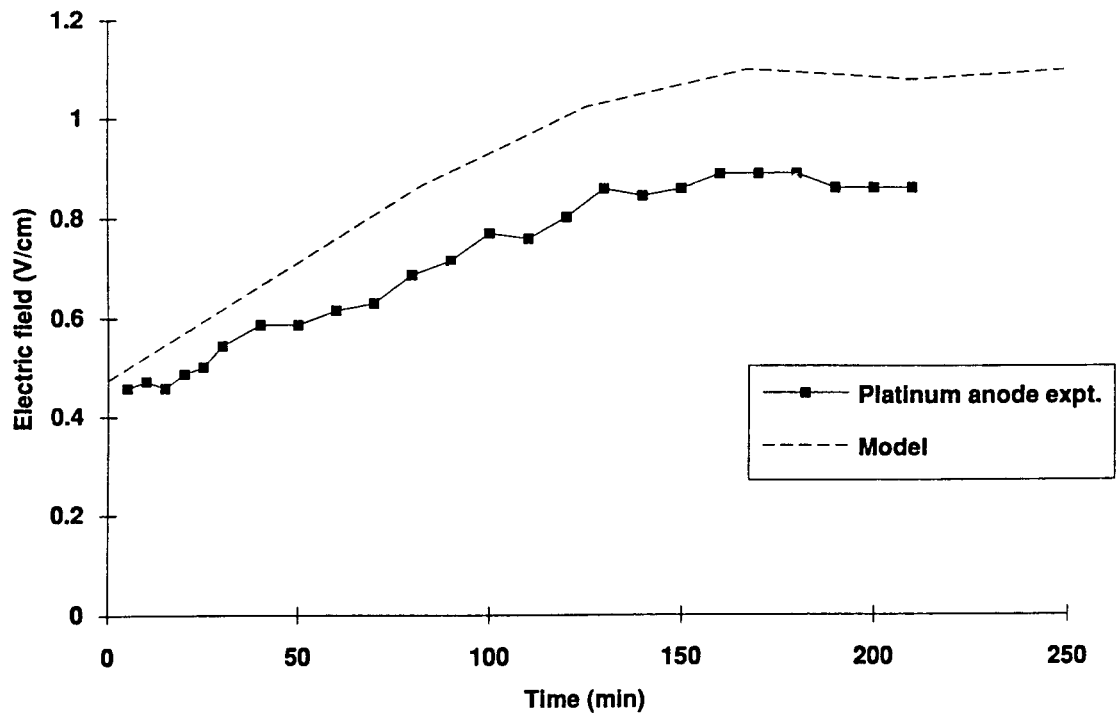
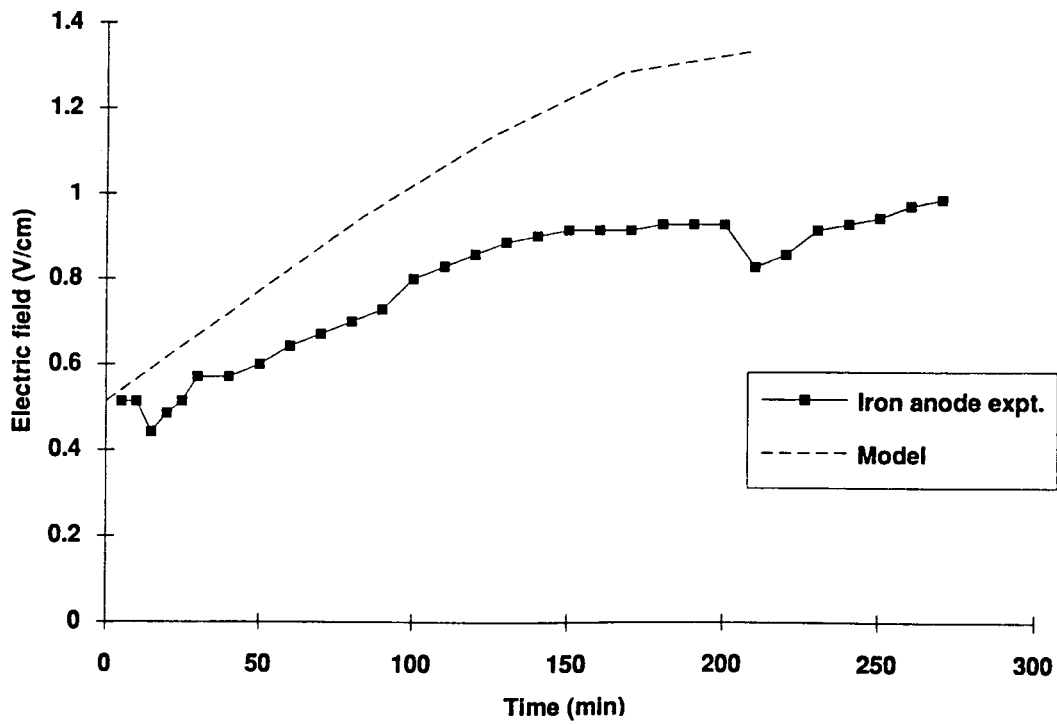


Figure 14d. Trajectory of high and low pH fronts for agar simulation with inert anode. Model parameters are listed in Table 5.



(a)



(b)

Figure 15. Model prediction of electric field in agar experiments for (a) inert anode and (b) iron anode.

When an iron anode is used in the agar experiments, the pH distribution is quite different. The model prediction for this case is shown in Fig. 16a. With an iron anode the expected electrode reaction is



Given the dissolution of iron instead of the production of H^+ at the anode, it is expected that the decrease in pH will be less when iron electrodes are used. The model indicates that a front characterized by pH~4 propagates from the anode when iron is used, which is compared with pH~2 when inert electrodes are used.

One interesting prediction by the model is a thin (~1 mm) pH~10 spike that also propagates from the anode. This pH spike is caused by the precipitation of ferrous hydroxide. While such a pH spike was not observed in the agar experiments, which used dye indicators to visualize the pH, it is not clear whether the experiment conditions would have permitted resolution on such a fine scale.

The pore water ions are shown in Fig 16b, and in this case include ferrous ions also. The ferrous ions migrate toward the cathode with the low pH front. After the fronts meet, at about 250 minutes, the ferrous ions accumulated at the low/high pH interface where ferrous hydroxide is precipitated. This precipitation is illustrated in Fig. 17 where the model prediction of the total iron distribution is plotted compared to the measured distribution in the agar after the experiment was completed. The spike at the 2-cm position coincides with the interface of the low and high pH regions. While the spatial resolution provided by the experiment is insufficient to compare the shapes of the predicted and measured iron distribution, the extent that the iron migrated into to agar is in good agreement. The propagation of the fronts is shown in Fig. 16d and agrees well with the experimental measurements.

The pH of the anode and cathode solutions for the agar experiments was also monitored and serves as another validation point for the model. Figures 18 a-b show the transient behavior of the anolyte and catholyte in the two experiments and compare them with the model predictions. Good agreement between model and experiment is apparent, and the effect of the iron anode on moderating the pH drop is obvious.

Pilot-scale simulation

The parameters used in the simulation of the Paducah field test are listed in Table 6. Those parameters not listed in Table 6 had the same values as listed in Table 5.

Table 6. Model Parameters Used in Numerical Simulation of Paducah Field Experiment.

Property	Variable	Value
porosity	n	0.4
tortuosity	τ	1.25
Soil density, kg m ⁻³	ρ	2.0·10 ⁺³
Specific surface area, m ² kg ⁻¹	A_s	3.0·10 ⁺⁵
Fraction adsorbed H ⁺ on soil surface	f	0.998
Fraction adsorbed Na ⁺ on soil surface	g	0.98
Initial NaCl concentration, molL ⁻¹	c_2, c_3	6.0·10 ⁻³
Concentration of H ⁺ exchange sites, molL ⁻¹	cec	1.70
Surface charge constant, Cm ²	σ_0	-2.73·10 ⁻¹
Electrode spacing, m	L	3.0

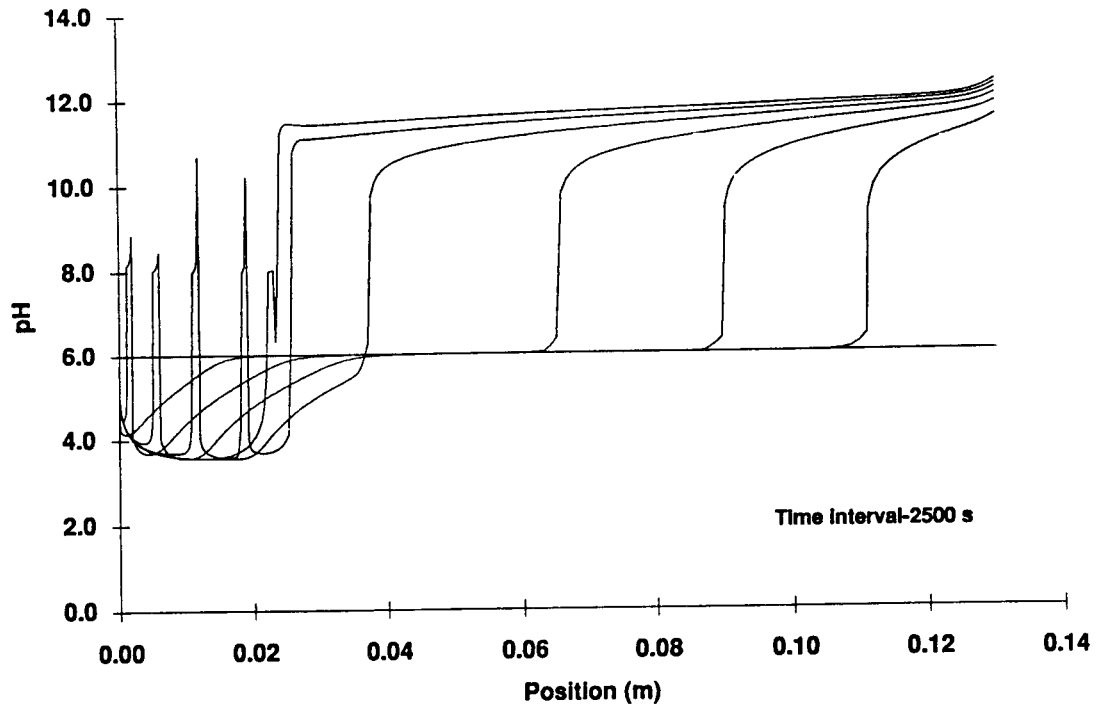


Figure 16a. pH distribution for agar simulation with iron anode. Model parameters are listed in Table 5.

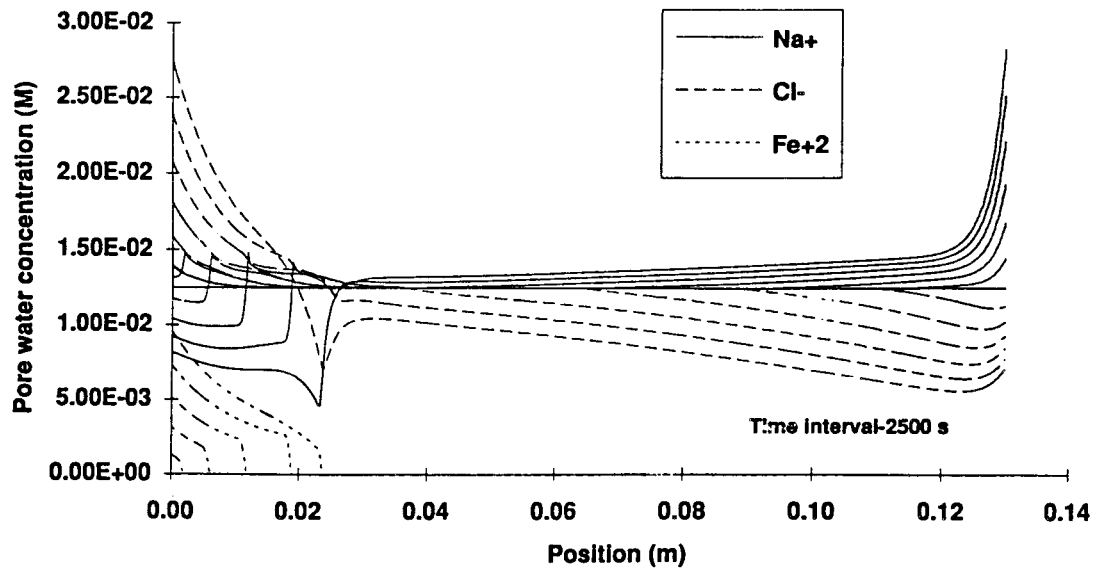


Figure 16b. Pore water ion distribution for agar simulation with iron anode. Model parameters are listed in Table 5.

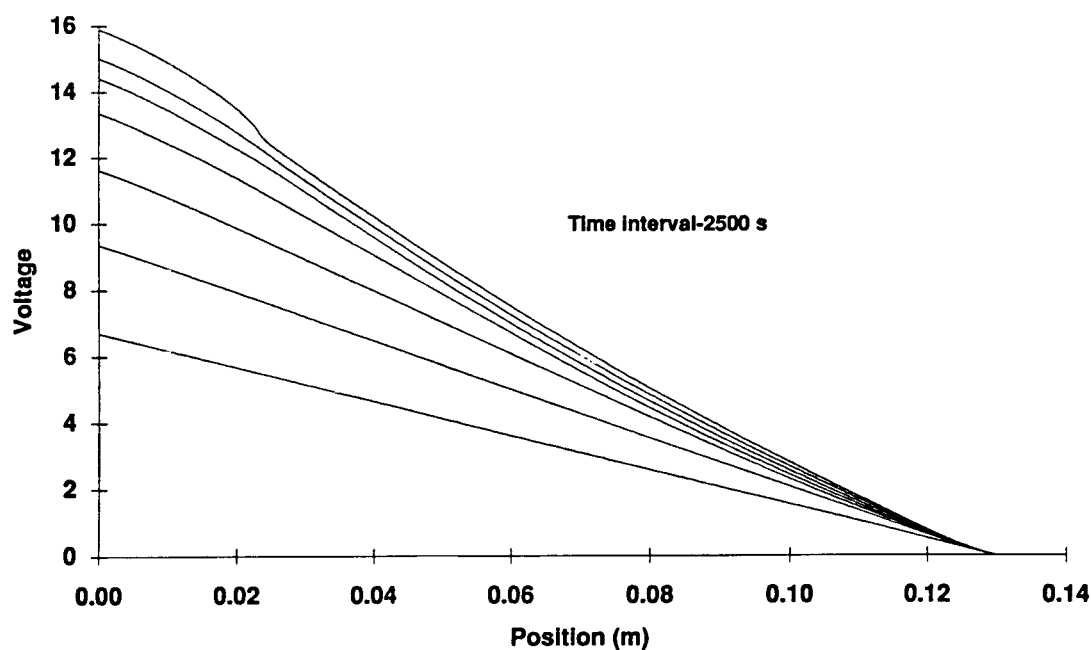


Figure 16c. Voltage profile for agar simulation with iron anode. Model parameters are listed in Table 5.

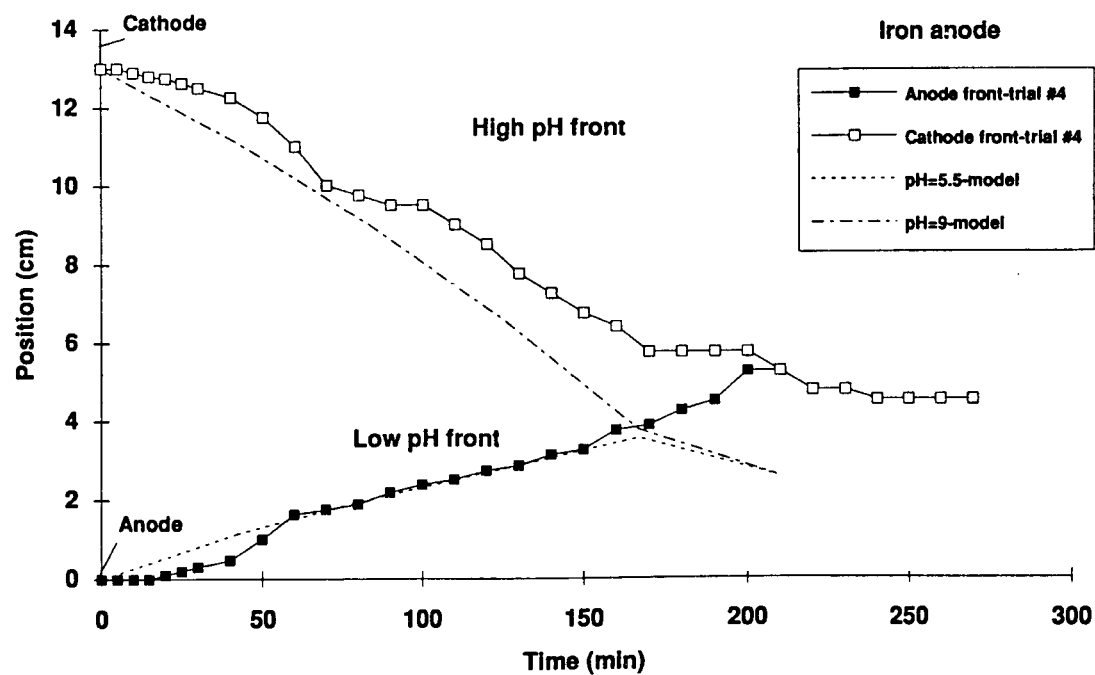


Figure 16d. Trajectory of high and low pH fronts for agar simulation with iron anode. Model parameters are listed in Table 5.

The titration curve for the H^+ absorbing capacity of the Paducah soil is

$$c_{H^+}^{ads} = 2.246 - 0.4399pH + 0.1099pH^2 - 1.201 \cdot 10^{-2} pH^3 + 3.934 \cdot 10^{-4} pH^4 \quad (23)$$

The buffering capacity of this soil is quite large. For example, the difference in the amount of H^+ adsorbed between $pH = 2$ and $pH = 12$ is 1.6 moles per liter of pore solution.

The three layer model in which ions are either in the neutral pore liquid, in the charge diffuse double layer, or adsorbed to the soil surface was used to describe the pH and concentration dependency of the soil zeta potential. Using the constraints that (i) the soil point of zero charge was $pH = 3$, (ii) at $pH = 7$ and

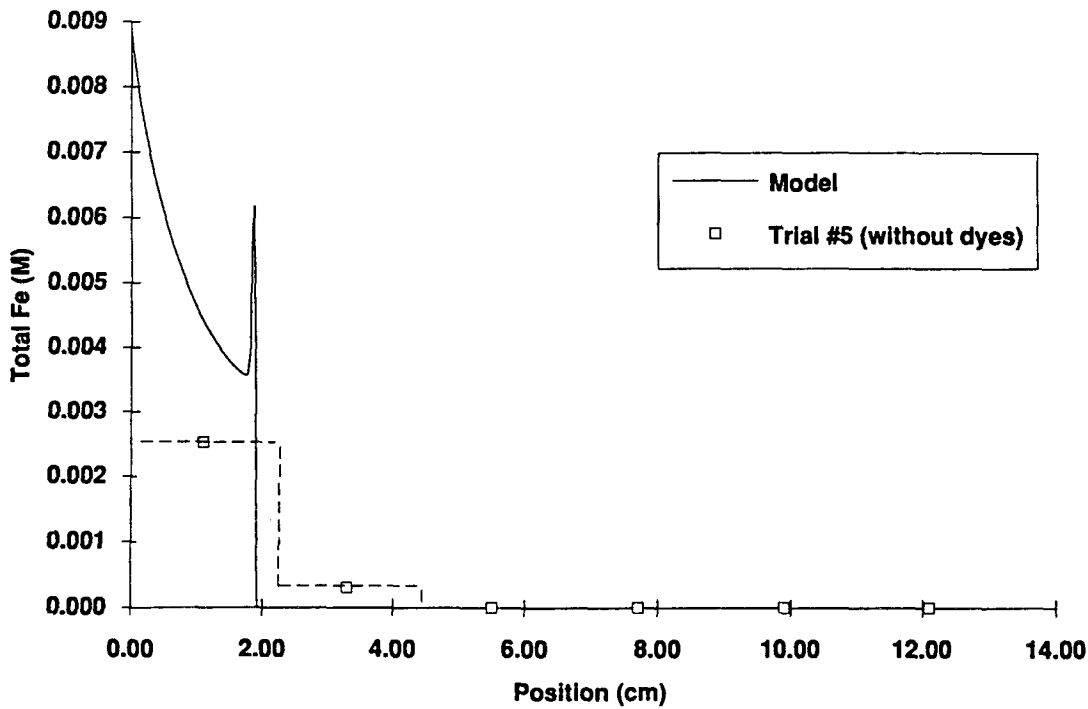
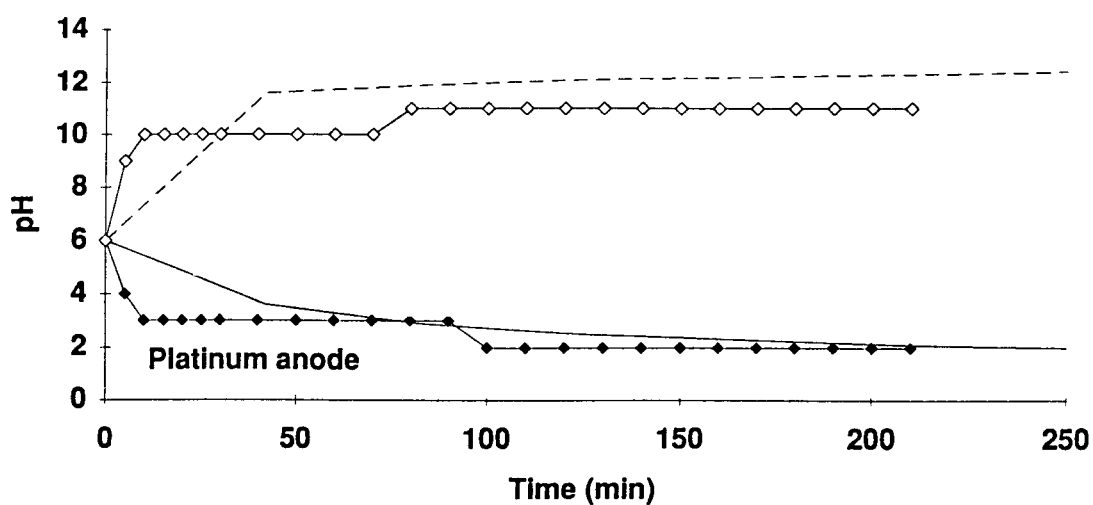
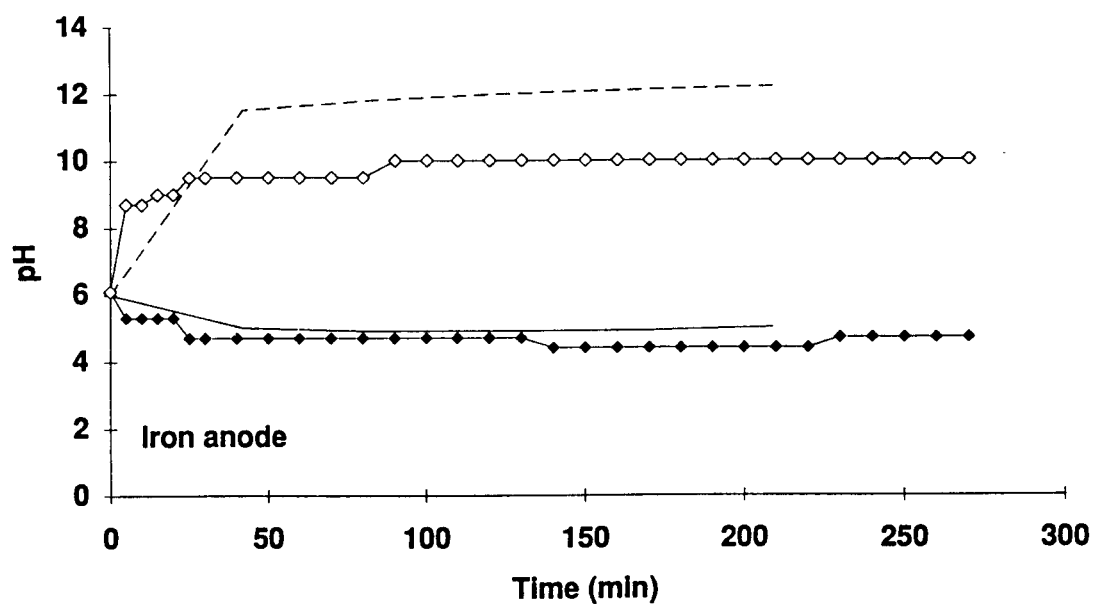


Figure 17. Comparison of model prediction and measured total iron distribution in agar experiments with iron anode.

pore solution ionic strength of 0.006 M, the zeta potential was -5.6 mv, and (iii) the soil electrical conductivity was $0.042 \Omega^{-1}m^{-1}$ at $pH = 7$ and ionic strength of 0.006 M, the model parameters were determined. The resulting constants were $f = 0.998$, $g = 0.980$, and $\sigma_0 = -0.273$. The model representation of the soil zeta potential is shown above in Fig. 12.



(a)



(b)

Figure 18. Comparison of experimental and predicted anolyte and catholyte pH behavior in agar experiments for (a) inert anode and (b) iron anode.

Simulations of the pilot test conditions were run for two cases: for inert anode material and for iron anodes. The pH and ion distributions predicted in the simulation for inert electrodes are shown in Fig. 19 a-d. It is clear that the buffering capacity of the soil limits the propagation of the low pH front from the anode to only a few centimeters after 35 days. The ions in the neutral pore liquid are also concentrated near the anode, and after 23 days, nearly all of the ions are removed from the bulk of the liquid. It should be noted that for consistency with the operation of the field test, the boundary conditions applied in these simulations allowed for the solution removed at the cathode to be introduced at the anode.

The deionization of the pore water would have led to very low currents if transport in the double layer were not included in the model. However current carried in the double layer accounted for nearly all of the current after about 23 days. The predicted system resistance for the pilot test, which had a $4.6 \text{ m} \times 4.6 \text{ m}$ cross-sectional area, is plotted vs time in Fig. 20. The model predicts that the system resistance will increase by about 20% regardless of electrode type. The fact that the measurements from the pilot test, also plotted in Fig. 20, show an actual decrease in resistance is attributable to temperature effects that have been addressed in the thermal model. The average temperature increase in the soil was about 20°C in the first 30 days of the pilot test, which would result in an estimated 40% decrease in soil resistivity, and if included in the chemical transport model would agree quite well with the pilot test data.

Because nearly all of the current is carried in the double layer, and the ionic strength of the double layer does not change significantly either spatially or temporally, the electric field, as shown in Fig. 21, is very uniform. The nonuniformity in the field at 11.6 days occurs because there are still significant ions in the neutral pore solution in the anode half of the soil.

The fourth case analyzed with the chemical transport model was the pilot test with iron dissolution as the anode reaction. The pH and ionic distributions are shown in Fig. 22a-d. In this case, the model actually predicted a rise in anolyte pH to about 7.5. The pH does not change significantly with the iron electrode because the chloride ions are neutralized by ferrous ions dissolved from the anode. As with the inert electrodes, the pH fronts resulting from anode reactions only migrate about 10 cm away from the anode because of the buffering capacity of the soil. Again, the ions in the neutral pore water solution accumulate near the anode, and after 23 days, nearly all of the current is carried in the double layer.

The electric potential distribution is shown in Fig. 23, along with data from the pilot test. Note again that the buffering action of the soil and the fact that the model accounts for current transport in the double layer results in a very uniform electric field. The electric potential data from the pilot test show some nonuniformities. However, potential distribution measured in the field changed very little with time, indicating that the nonuniformities are attributable to soil heterogeneity rather than to redistribution of ions by electromigration.

Finally, the distribution of TCE is plotted in Fig. 24. The four treatment zones are assumed to be perfect sinks for the TCE. The initial pore water concentration of TCE was 4.4 mM or about 600 ppm. Assuming saturated soil with 0.4 porosity and a soil density of 2000 kg m^{-3} , the initial TCE concentration on a soil weight basis was 120 ppm. At this concentration, adsorption of TCE on the soil is negligible. The model predicts 91% removal of the TCE after 0.8 pore volumes have passed between treatment zones.

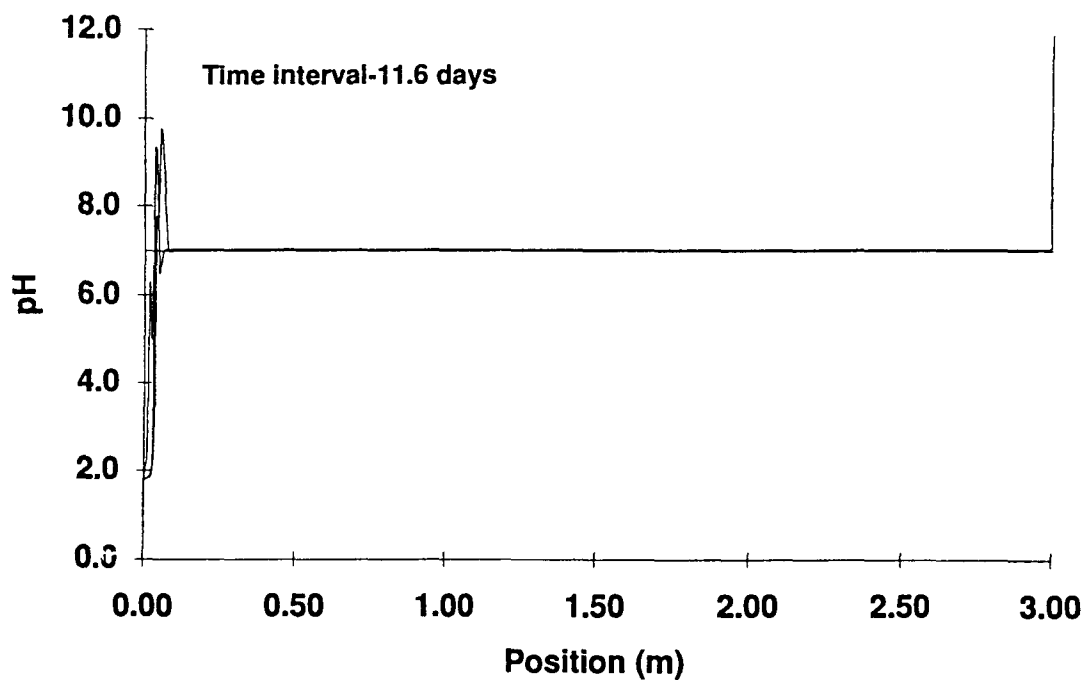


Figure 19a. pH distribution (0-3 m) for simulation of Paducah field test with inert anodes. Time interval between profiles is 11.6 days.

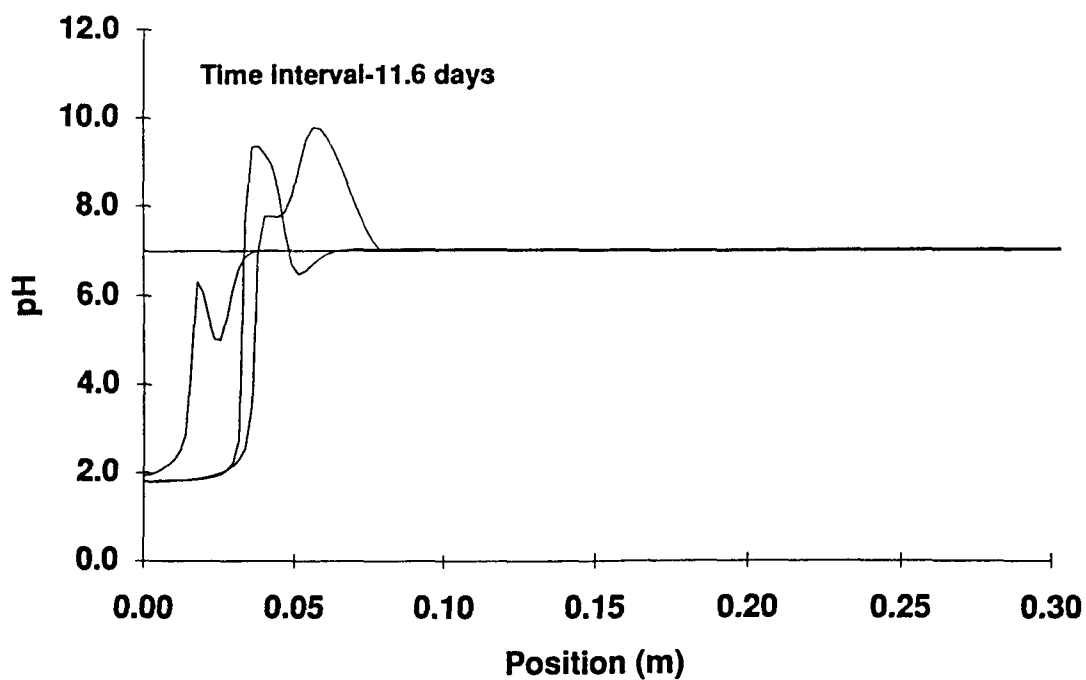


Figure 19b. pH distribution (0-0.3 m) for simulation of Paducah field test with inert anodes. Time interval between profiles is 11.6 days.

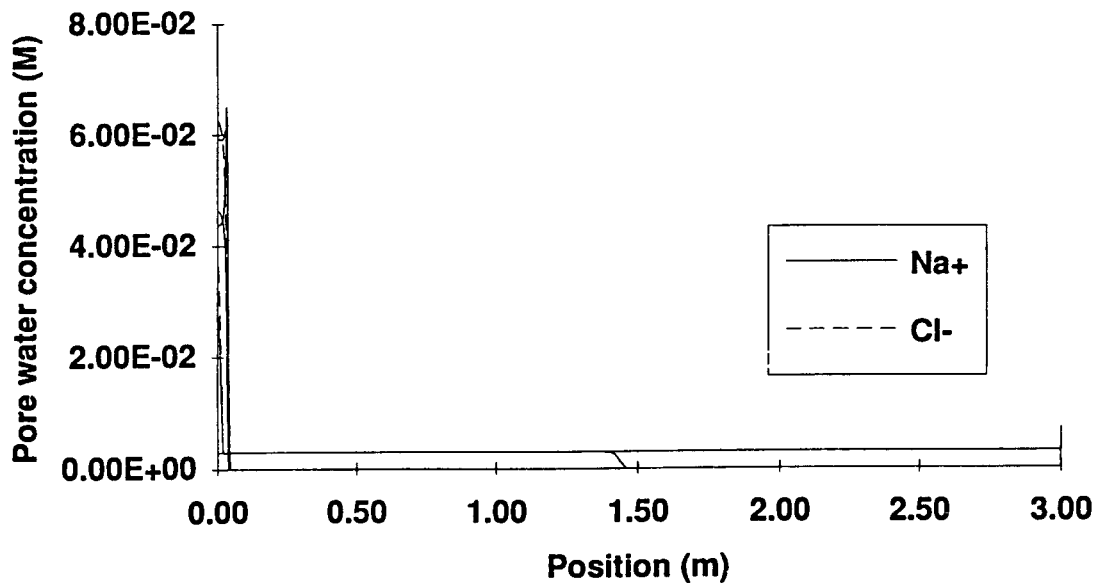


Figure 19c. Pore water ion distribution (0-3 m) for simulation of Paducah field test with inert anodes. Time interval between profiles is 11.6 days.

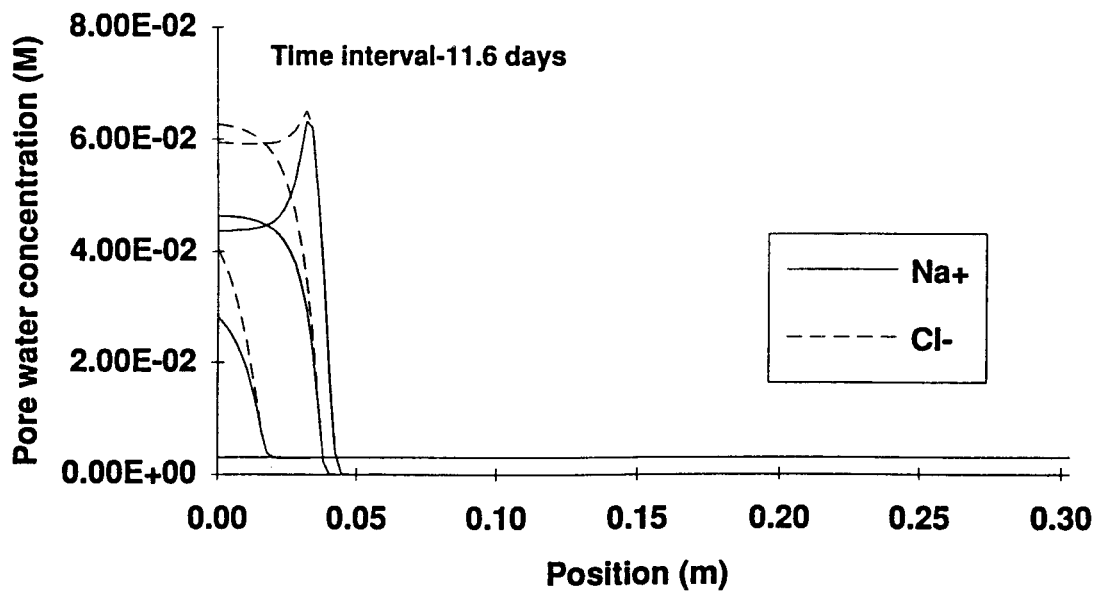


Figure 19d. Pore water ion distribution (0-0.3 m) for simulation of Paducah field test with inert anodes. Time interval between profiles is 11.6 days.

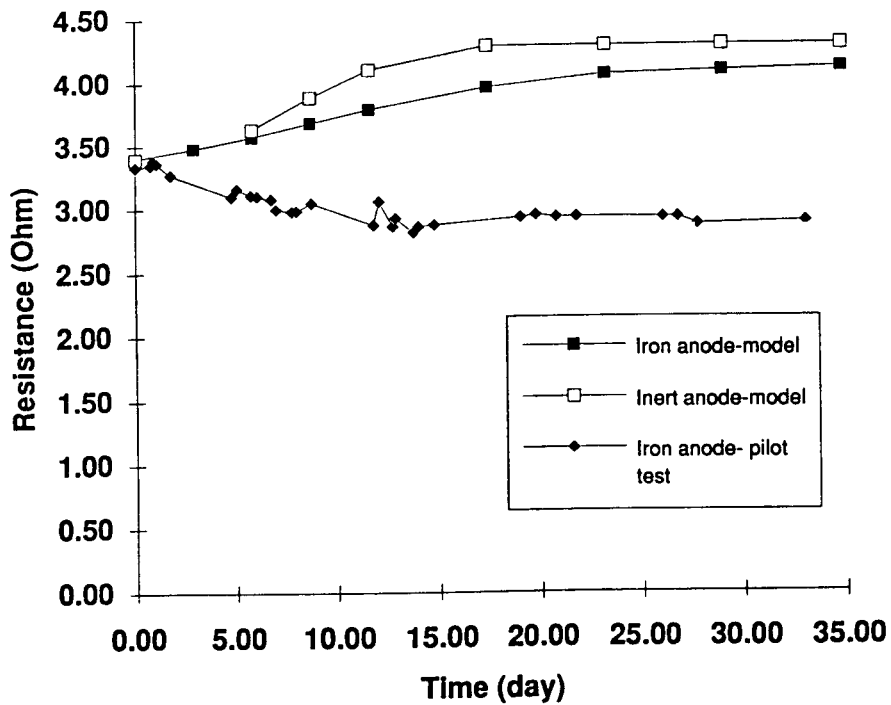


Figure 20. System resistance predicted by model simulation and experimental data of Paducah pilot test. Decrease in pilot test resistance is attributable to temperature increases that increase the soil conductivity.

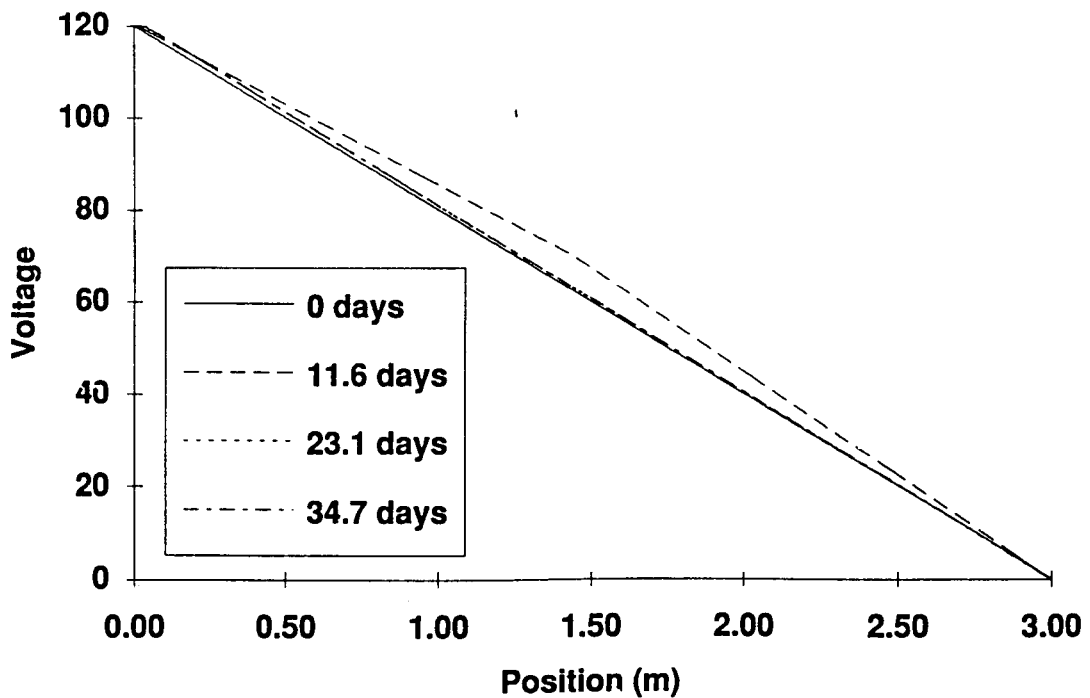


Figure 21. Voltage distribution for simulation of Paducah field test with inert anodes.

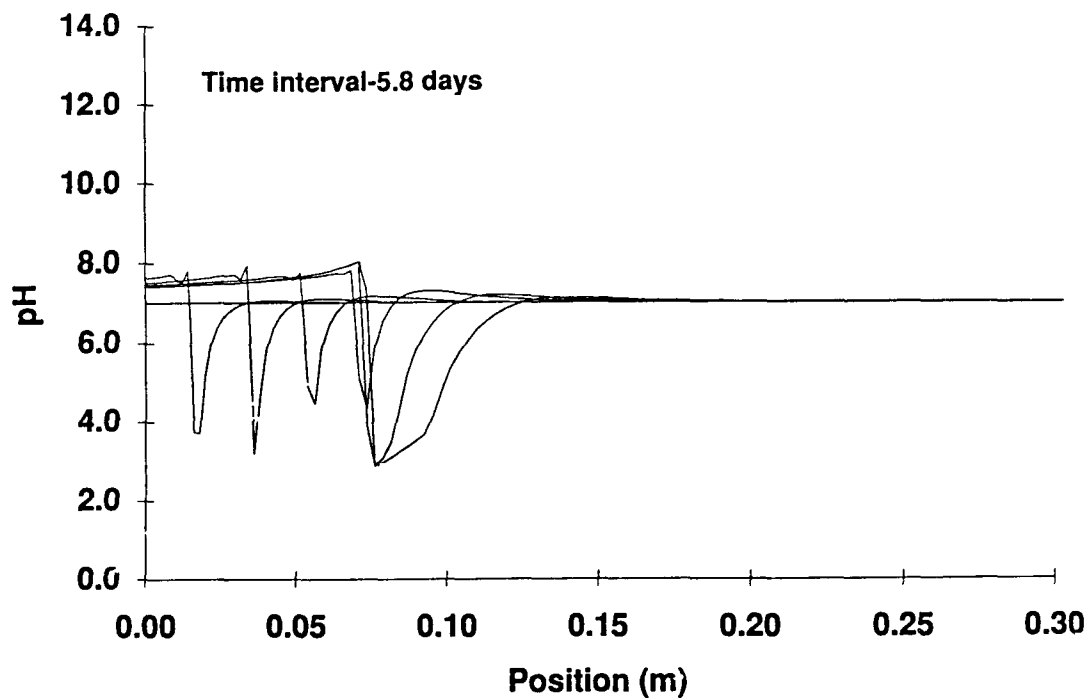


Figure 22a. pH distribution (0-0.3 m) for simulation of Paducah field test with iron anodes. Time interval between profiles is 5.8 days.

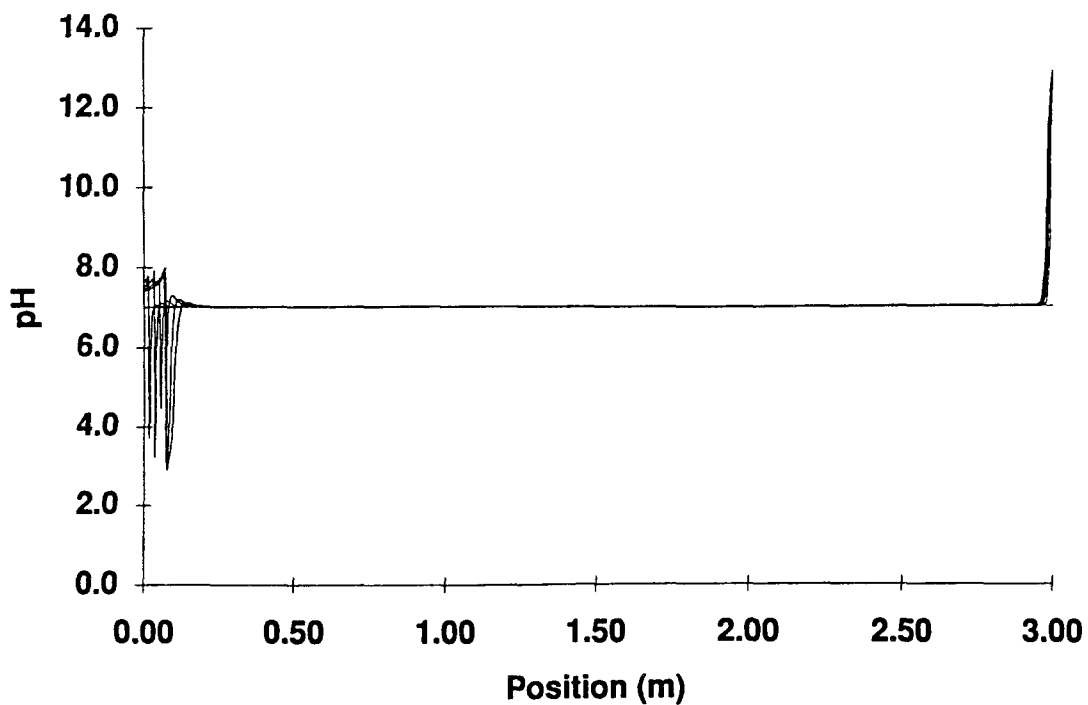


Figure 22b. pH distribution (0-3.0 m) for simulation of Paducah field test with iron anodes. Time interval between profiles is 5.8 days.

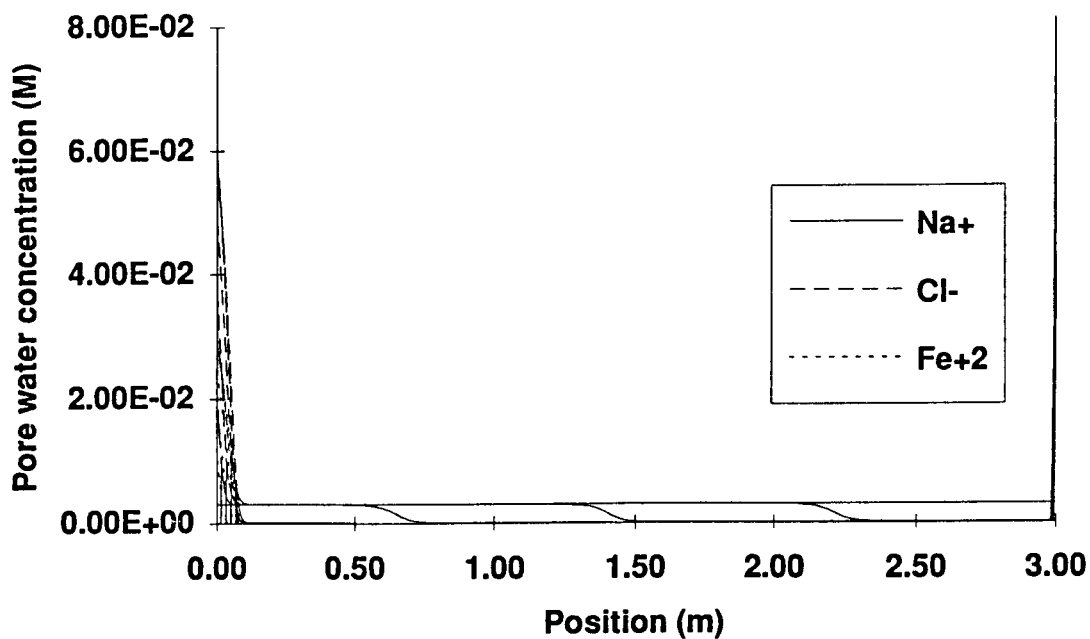


Figure 22c. Pore water ion distribution (0-3 m) for simulation of Paducah field test with iron anodes. Time interval between profiles is 5.8 days.

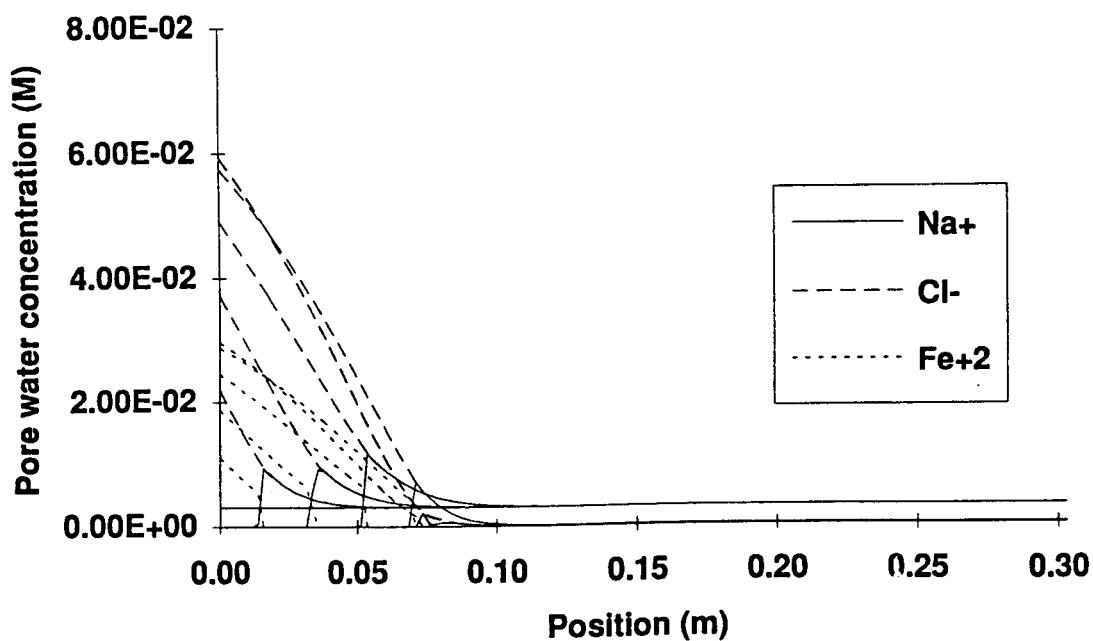


Figure 22d. Pore water ion distribution (0-0.3 m) for simulation of Paducah field test with iron anodes. Time interval between profiles is 5.8 days.

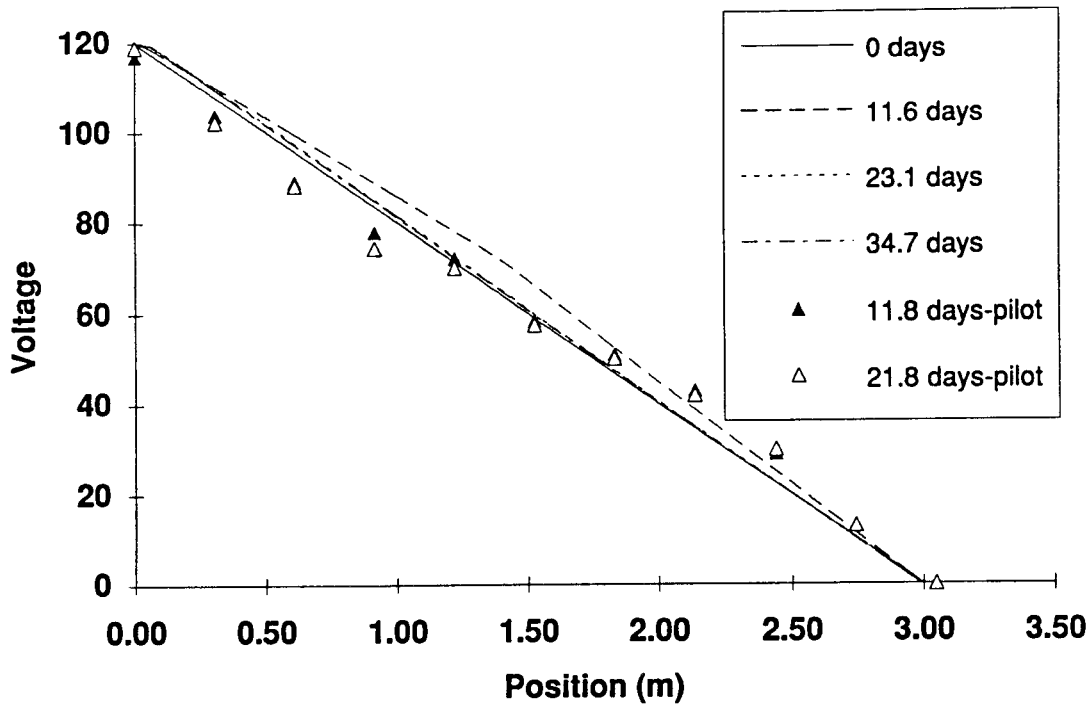


Figure 23. Voltage distribution for simulation of Paducah field test with iron anodes and measured voltages from field test.

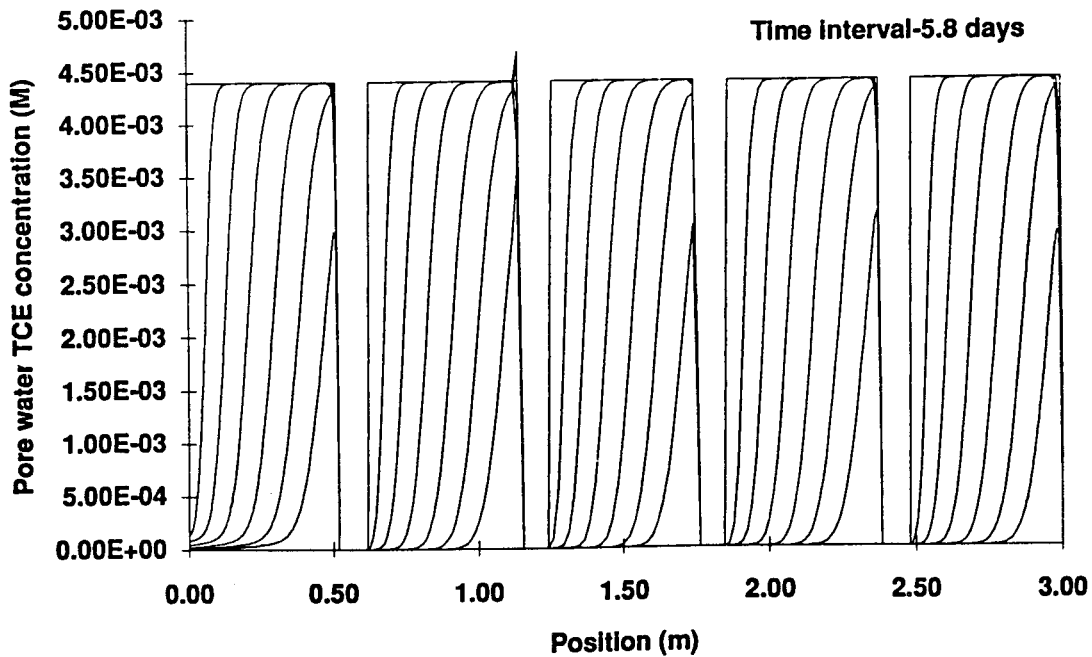


Figure 24. Predicted TCE distribution for simulation of Paducah field test with iron anode. Time interval is 5.8 days. Treatment zones are modeled as perfect sinks.

Conclusions

The model developed here is based on previous models of chemical transport in electrokinetic remediation^{1,10,13} and has been augmented to include the pH buffering capacity of soil, zeta potential dependence on pH and ionic strength, and transport of ions in the double layer. The model assumes that species can be in one of three layers: the neutral bulk solution, the electrically charged double layer, or adsorbed to the soil surface. Selective partitioning of ions between the soil surface and the double layer leads to the zeta potential dependency on pH and ionic strength.

The model has been validated with laboratory experiments on agar gels and with results from the Paducah pilot test. The model accurately predicts the migration of low and high pH fronts from electrodes, the effects of using iron anode on reducing the pH drop in the anolyte, and the uniform electric field observed in the pilot test. The model predicts that most of the current is carried in the double layer in the Paducah soil. While this result could not be directly verified in the Paducah field test, the implications of field uniformity and small changes in overall resistivity are consistent with the model's predictions.

The results of this model and the corroboration by experimental measurements support some key assumptions made in the thermal model. Specifically, in the thermal model, chemical species transport was neglected. Therefore, redistribution of ions leading to nonuniformities in Joule heating was not accounted for. Given the uniform electric field predicted by the model, this assumption appears to be valid. The buffering capacity evidently confines regions of high ionic strength near the electrodes, and the current transport in the double layer prevents low conductivity regions from dominating the overall system.

3. Analysis of Electrode Geometry and Heterogeneity

Comparison of Wells and Plates

To ensure the interception of all contaminants in the Lasagna[®] process, it is essential to have treatment zones that completely span the contaminated region. However, it may not be necessary to have electrodes installed in the same manner. Because cost savings may be realized by installing cylindrical electrodes (pipes) in a periodic array, a thermal analysis of possible emplacement geometries was conducted. When planar electrodes are used, the hottest region is near the midpoint between anode and cathode. With cylindrical electrodes, the hottest region may be at the electrode, because electric current and joule heating are concentrated at these electrodes. In the analysis that follows, FIDAP[®] was used to simulate a three-dimensional geometry in which electrodes were sunk 5 m deep and were placed periodically in alternating rows of anodes and cathodes. The anode rows were parallel to, and spaced 10 m from, the cathodes rows. The anode-anode and cathode-cathode distance was 1 m on center. Two current densities, 0.4 and 0.8 A/m², and two electrode diameters, 0.1 and 0.05 m, were considered. The current densities are based on the current flowing between a single anode-cathode pair divided by the distance between anodes (1 m) times the electrode depth (5 m). Electroosmotic convection was not included in these calculations because its effect is small (Peclet number = $u_{eo}L\rho_w c_w/k \approx 0.1$) and neglecting convection greatly simplifies the computation. The temperature dependence of electrical conductivity was included.

The thermal boundary conditions were constant temperature (20°C) at the surface and at 8 m depth. The electrodes were thermally insulated. In Fig. 25, the maximum temperature rise for the four cases is plotted versus time. In each case the maximum temperature occurs at the electrodes. It is apparent that the maximum temperature is higher for smaller electrodes when operated at a given current because the current density in the vicinity of the electrode drops off as 1/r, and is therefore relatively large for small diameter electrodes.

The time for remediation depends on the spacing of treatment zones. If a 1-m spacing and soil properties of $k_{eo} = 10^{-9} \text{ m}^2 \text{ V}^{-1} \text{ s}^{-1}$ and $\sigma(20^\circ\text{C}) = 0.024 \text{ S/m}$ are assumed, then the time for one pore

volume to be purged is 690 days for 0.4 A/m² and 350 days for 0.8 A/m². Therefore, these current densities and temperatures are probably on the low end of what would be used in the field. However, given this geometry, one could not increase the current density much above 1.2 A/m² without boiling water at the electrode. Conversely, since the hottest region is at the electrode, circulation of the electrolyte with appropriate cooling could be used to prevent water boiling.

The applied voltage decreases with time because of the effect of temperature on electrical conductivity. These voltages are plotted in Fig. 26 for the four cases analyzed. It is important to note that by increasing the electrode diameter from 5 to 10 cm, the applied voltage, and hence the power, decreases by about 10%. Therefore, there is a tradeoff between energy costs and electrode material and installation costs that must be considered.

In the case of iron anodes, dissolution of the iron from electrochemical reactions requires that there is enough iron to last the duration of the remediation. This issue, rather than thermal effects, may determine the minimum anode diameter. Assuming that the electrode reaction is $Fe^0 \rightarrow Fe^{2+} + 2e^-$, one can show that the minimum cross-sectional area, A_e , per unit length of electrode row, b , is given by

$$\frac{A_e}{b} = \frac{M_w}{\rho} \frac{i}{Fz} t_r \quad (24)$$

where M_w is the molecular weight of iron (55.8 g/mol), ρ the density of iron (7.6 g/cc), i the current density, F Faraday's constant (96,500 C/mol), z the valence change of the electrode reaction (2), and t_r the remediation time. For a cylinder A_e is $\pi d^2/4$, and for planar electrodes A_e is $w \cdot b$, where w is the width. This calculation shows that for $i = 0.8$ A/m², $t_r = 700$ days, and $b = 1$ m, the minimum diameter of a solid iron electrode would be 4.8 cm, whereas the minimum thickness of a plate of solid iron would be 0.18 cm. The actual iron rod would have to be substantially thicker than 4.8 cm to ensure mechanical and electrical integrity and to allow for fluid flow. Therefore the 0.1-m case simulated above may be a feasible scenario. If the anode were a pipe 0.1 m in diameter and had a wall thickness of 2.7 cm, it would have twice the amount of iron needed, based on the equation and assumptions above.

In summary, cylindrical electrodes may be appropriate for anodes, because they do not intercept the flow. If used as cathodes, a planar treatment zone in their vicinity would probably be required. The cylindrical electrodes can operate at reasonable current densities without boiling water. Because the hottest region is at the electrode, cooling schemes could be used to operate at higher current densities. If iron anodes are used, they will have to be quite massive, and may not be economical compared to planar panels. However, anodes made of inert materials may be smaller and inexpensive to install.

Analysis of a buried metal object

This section addresses the influence of the buried steel plate on the electric field in the Lasagna field test. FIDAP, a commercial finite element code, was used to analyze the electric field with and without the buried steel plate. The geometry and boundary conditions used represent a worst case scenario in that a two-dimensional model was used (i.e., it is more like a buried block of steel that goes all the way down), and no isolation effect of the insulation barriers was assumed (i.e., the only objects in the ground are the electrodes and the plate). The steel plate was assumed to be 15 ft by 7 ft with the northernmost corner of the plate 6 in. outside the test zone.

The results of the calculations are that the plate has little effect on the electric field between the electrodes, even in the worst case scenario. The equipotential lines are shown in Fig. 27 for the case with the plate. There is some distortion of the field near the plate, but its effects on the test zone between the electrodes are minimal. The only significant effect is that the current in the case with the plate is about 6% higher than with no plate.

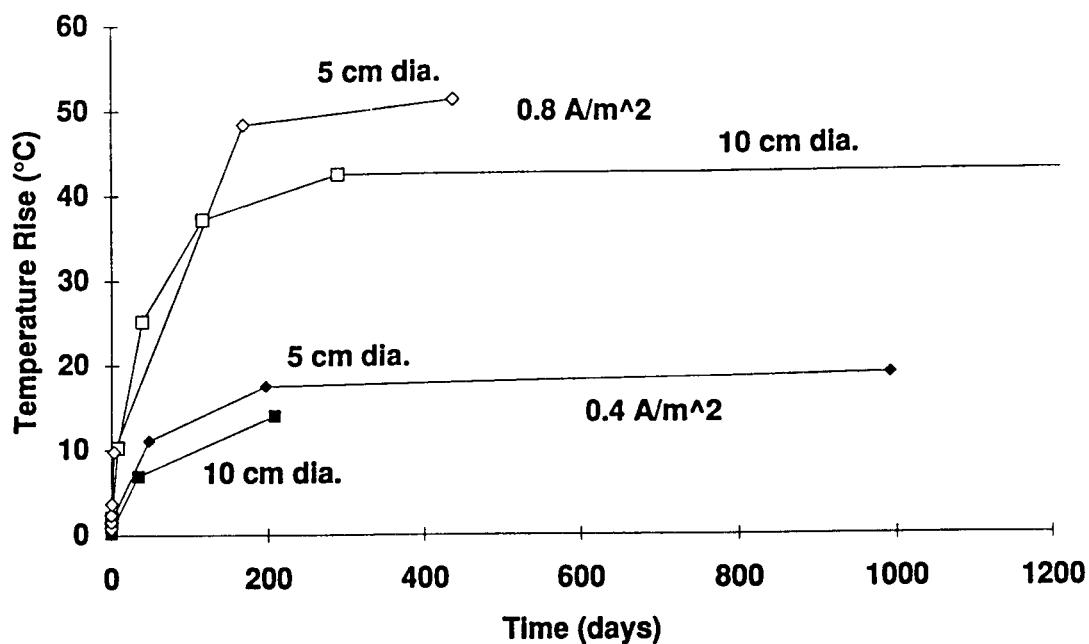


Fig. 25. Maximum temperature rise vs time. Anode rows are 10 m from cathodes rows; inter-anode and inter-cathode spacing is 1 m; $\sigma(20^{\circ}\text{C}) = 0.024 \text{ S/m}$.

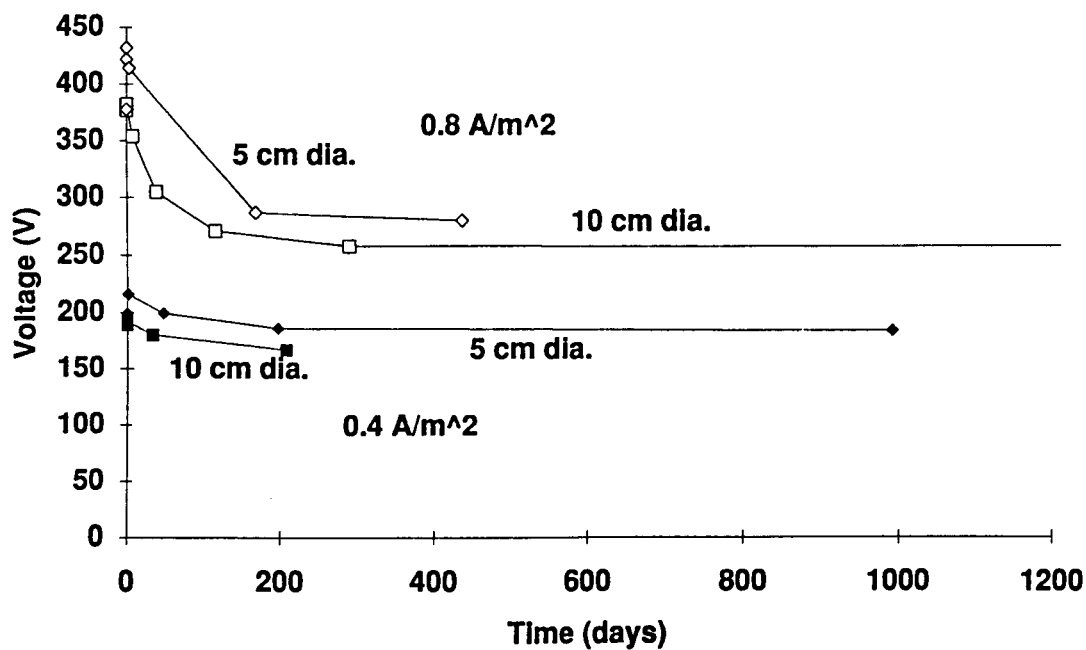


Fig. 26. Applied voltage vs time. Anode rows are 10 m from cathodes rows; inter-anode and inter-cathode spacing is 1 m; $\sigma(20^{\circ}\text{C}) = 0.024 \text{ S/m}$.

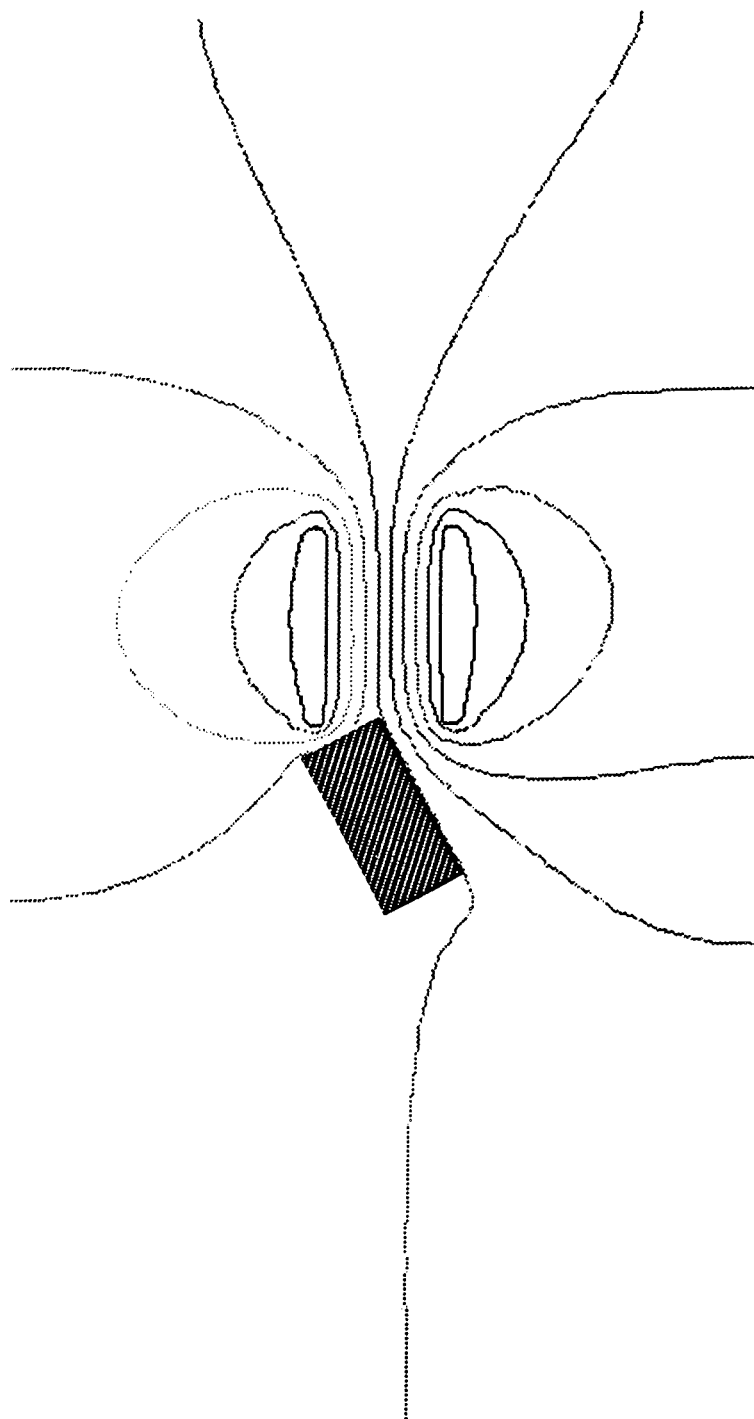


Fig. 27. Equipotential lines in two-dimensional representation of the pilot test geometry with a buried steel pit.

References

- [1] Shapiro, A.P., Renaud, P.C., Probstein, R.F. ,*PCH, PhysicoChem. Hydrodyn.* 1989, *11*, 785.
- [2] Alshawabkeh, A.N., Acar, Y.B., *J. Environ. Sci. Health*, 1992, *A27*(7), 1835.
- [3] Eykholt, G.R., Daniel, D.E.,*J. Geotechnical Eng.* 1994, *120*(5), 797.
- [4] Jacobs, R.A., et al., *J. Environ. Sci. Health*, 1994, *A29*(9), 1933.
- [5] Hicks, R.E., Tondorf, S.,*Environ. Sci. Technol.*, 1994, *28*(12), 2203.
- [6] Probstein, R.F., *Physicochemical Hydrodynamics, An Introduction*, 1994, 2nd edition, John Wiley & Sons, Inc., New York, p. 197.
- [7] Weast, R.C., ed. *Handbook of Chemistry and Physics*, 1972, The Chemical Rubber Co., Cleveland, p. F-36.
- [8] Gurney, R.W., *Ionic Processes in Solution*, 1953, Dover Publications, New York, p. 69.
- [9] Shapiro, A.P., Ph.D. Thesis, Massachusetts Institute of Technology, 1990.
- [10] Jacobs, R.A., Probstein, R.F., *AIChE J.*, submitted 1995.
- [11] Dzenitis, J., Probstein, R.F., Presented at Emerging Technologies in Hazardous Waste Management VII, American Chemical Society, Atlanta, GA, Sept. 17-20, 1995.
- [12] Hiemenz, Principles of Colloid and Surface Chemistry, p. 370.
- [13] Shapiro, A.P., Probstein, R.F., *Environ. Sci. Technol.*, 1993, *27*(2), 283.
- [14] Saville, D.A., Palusinski, O.A., *AIChE J.*, 1986, *32*, 207.

D. Acronyms and Abbreviations

A563	Ambersorb 563 sorbent (Rohm and Haas)
AS	air stripper or air stripping
BPL	activated carbon (Calgon)
BTC	breakthrough curve
BTEX	benzene, toluene, xylenes
CCl ₄	carbon tetrachloride
CH ₂ Cl ₂	methylene chloride, dichloromethane
COD	chemical oxygen demand
CSTR	continuous stirred-tank reactor
CVOC	chlorinated volatile organic compound
D	desorbing gas flow rate
d _p	diameter of particle
D _c	diameter of column
DCM	methylene chloride, dichloromethane
D.O.	dissolved oxygen
DOE	Department of Energy
ΔP	pressure drop
ΔP/L	pressure drop per unit length
EBCT	empty bed contact time
ECD	electron capture detector
EPA	Environmental Protection Agency
EPCM	engineering, procurement and construction management
F	feed flow rate
FBR	fluidized-bed reactor
FID	flame ionization detector
GAC	granular activated carbon
GC	gas chromatography
GE	General Electric Company
GEP	GE Plastics
H	Henry's law constant
HCl	hydrochloric acid
HRT	hydraulic retention time

HW	hazardous waste
HWTSD	hazardous waste toxic substance disposal
ID, I.D.	inside diameter
INEL	Idaho National Engineering Laboratory
K	constant in Freundlich equation (Chapter 3)
K _p	equilibrium constant (aqueous phase - Chapter 8)
K _v	equilibrium constant (vapor phase - Chapter 8)
L _c	length of column, bed height
MC, MeCl ₂	methylene chloride, dichloromethane
MeOH	methanol
MTZ	mass transfer zone
N ₂	nitrogen
n, 1/n	constant in Freundlich equation (Chapter 3)
NA	not available
O&M	operating and maintenance
OD	optical density
PAS	phosphate-ammonium salts
PCE	perchloroethylene, tetrachloroethylene
PVC	polyvinyl chloride
q	sorption capacity (g _{CVOC} /g _{sorbent})
R ₂ A	a rich agar medium
RD	remedial design
RH	relative humidity
RI/FS	remedial investigation/ feasibility study
ROD	record of decision
SVE	soil vapor extraction
T _m	melting temperature
TCE	trichloroethylene
TSDF	toxic substance disposal facility
TSS	total suspended solids
VOC	volatile organic compound
VSS	volatile suspended solids
WWTP	wastewater treatment plant
XU, XUS	Dow XUS sorbent (Dow Chemical)

E. Units

BTU	British thermal unit
C, °C	Celsius, degrees Celsius
cc	cubic centimeters
cfu, CFU	colony-forming units
cm	centimeters
d, D	days
deg	degrees
F, °F	Fahrenheit, degrees Fahrenheit
f, ft	feet
g	grams
gal, GAL	gallons
GJ	giga joules (10^9 joules)
gpm, GPM	gallons/minute
h, hr	hours
hp, HP	horsepower
in	inches
in Hg (" Hg)	inches of mercury
k, K	thousand
kcal	kilocalorie
kg	kilograms
kw, KW	kilowatts
kw-hr, KWhr	kilowatt-hour
l, L	liters
lb, lbs	pound(s)
M	molar (moles/liter)
m	meter
mg	milligrams
MGD	million gallons/day
min	minutes
ml, mL	milliliters
mM	millimolar (millimoles/liter)
MM	million
mm	millimeters

mmol, mmole(s)	millimole(s)
mol	mole(s)
mw, MW	molecular weight
N	normal (equivalents/liter)
ppb	parts per billion
ppm, ppmw	parts per million (by weight)
ppmm	parts per million (molar)
ppmv	parts per million (by volume)
psi	pounds per square inch
psia	pounds per square inch -- absolute
psig	pounds per square inch -- gauge
sccm, SCCM	standard cubic centimeters/minute
SCF	standard cubic feet
scfh, SCFH	standard cubic feet/hour
scfm, SCFM	standard cubic feet/minute
sf	square foot
SLPM	standard liters / minute
μg	micrograms
μl, μL	microliters
μm	micrometers
μM	micromolar (micromoles/liter)
μmol, μmole(s)	micromole(s)
yr	year
"	inches
'	feet
#	pounds